Microstructure understanding of high Cr-Ni austenitic steel corrosion in high-temperature steam

Zhao Shen[1], Jianqiang Zhang[2], Shengchuan Wu[3,*], Xiaonan Luo[4], Benjamin M. Jenkins[4], Michael P. Moody[4], Sergio Lozano-Perez[4], Xiaoqin Zeng[1,*]

[1] National Engineering Research Center of Light Alloy Net Forming and State Key Laboratory of Metal Matrix Composites, School of Materials Science and Engineering, Shanghai Jiao Tong University, Shanghai, 200240, China

[2] School of Materials Science and Engineering, University of New South Wales, Sydney, NSW 2052, Australia

[3] State Key Laboratory of Traction Power, Southwest Jiaotong University, Chengdu 610031, China

[4] Department of Materials, University of Oxford, Parks Road, OX1 3PH Oxford, UK

Abstract: The microstructure and microchemistry of the oxide scales formed on Fe-21Cr-32Ni and Fe-17Cr-9Ni steels after exposure to deaerated high-temperature high-pressure steam at 600 °C for 1500 h have been analysed and compared by several advanced characterization techniques. By comparing the oxide scales formed at different-stages of exposure, it is shown that Fe-21Cr-32Ni steel was internally oxidized at the early-stage, and then an external oxide scale was developed together with an inner chromia band under the internal oxidation zone. In comparison, Fe-17Cr-9Ni steel was internally oxidized together with an external Fe-rich oxide scale during the entire experimental period. The thicknesses of the internal oxidation zone of Fe-21Cr-32Ni and Fe-17Cr-9Ni steels were ~7 and ~70 μm, respectively. Further characterisation revealed that the internal oxidation zone contained (Cr, Fe, (Ni))$_3O_4$ and nanoscale nickel networks, together with numerous nano-pores. The effects of these structures on mass transfer and reaction product formation were discussed, in connection with the alloy composition and the formation of the chromia layer.

Key words: High Cr-Ni austenitic steel; Internal oxidation; Multilayers; Transmission electron microscopy; Transmission Kikuchi diffraction.

1. Introduction

Due to their low cost, good mechanical properties, reasonable corrosion resistance, and low irradiation-induced void swelling, ferritic-martensitic (F-M) steels have been widely used as heat-resisting materials in the petrochemical industry, aerospace sector, conventional fossil fuel power plants, and nuclear power industry [1-5]. To further increase the thermal efficiency and reduce carbon emissions, increasing the operating temperatures has been a widely accepted strategy, especially in the power generation systems, where water is used as a heat transfer medium [6-12]. However, the corrosion resistance of F-M steels decreases significantly at temperatures above 600 °C in the environments containing water vapour [13-20]. The thickening and exfoliation of the surface oxide scales formed on the structural materials in the power generation systems may block the coolant flow and scratch the turbine blades [2], which is of a great concern for the safe long-term operation of the advanced power generation systems, such as the supercritical water-cooled reactor (SCWR) and the ultra-supercritical fossil fuel power plants [8-12]. Consequently, substitutional materials are required to replace the F-M steels in the advanced power generation systems.

Due to the increased contents of Cr and Ni in the Fe-Cr-Ni austenitic steels, they exhibit much higher corrosion resistance than that of the F-M steels in the high-temperature steam [9, 12, 14, 19, 21-31]. In addition, austenitic steels offer a better creep resistance for higher temperature application. Hence, the F-M steels have been partially replaced by the Fe-Cr-Ni austenitic steels in the advanced power generation systems. For austenitic steels, there are two important features which will affect their oxidation processes. Chromium diffusion in austenite is much slower than that in F-M steels which affects the critical chromium content required for the formation of a protective chromia scale. The high content of nickel in austinites is expected to play an important role in the overall corrosion process because of a significant lower thermodynamic driving force for Ni oxidation than that for Cr or Fe in the high-temperature steam environment. In the studies of the corrosion of Fe-based steels in high-temperature environments, multi-layered surface oxide scale is frequently observed [9, 13, 14, 17-19, 22, 24-28, 32-54]. The corrosion behaviours of these steels in high-temperature steam are very similar to that in carbon dioxide [55-59] and liquid metals [60-63] where low partial pressure of oxygen is ensued. Hence, the corrosion mechanisms of Fe-based steels in these different oxidation mediums are generally believed to be similar [64-72]. This multi-layered oxide scale normally contains both outer oxides above the original metal surface and inner oxides below this layer. This phenomenon can be attributed to both cation outward diffusion and oxygen inward diffusion. Clearly, the change of Cr diffusion and high content of Ni in austenitic steels will change the steel corrosion behaviour significantly.

Although the austenitic steels are generally more corrosion-resistant than the F-M steels due to their higher contents of Cr and Ni, it is reported that compared with the commonly-used 304/316 steels, in which the content of Cr is lower than 18 wt.% and Ni lower than 15 wt.%, further increase of Cr and Ni contents in the austenitic steels, such as 800H alloy (Fe-21Cr-32Ni) [31, 73-79], 310 steel (Fe-25Cr-23Ni) [80-82], and HR3C (Fe-25Cr-21Ni) [83-85], could further increase their corrosion resistance at high-temperatures. The corrosion behaviours of high Cr-Ni austenitic steels have been extensively studied [31, 73-85]. The increased corrosion resistance in these kinds of steels is generally attributed to the increased content of Cr, which is supposed to facilitate the formation of a more compact Cr-rich oxide scale. To date, a mechanistic understanding of the superior corrosion resistance of the high Cr-Ni austenitic steels at high-temperatures remains elusive due to the difficulties in collecting the requisite experimental scale of observations (micro-to-atomic). Although a general understanding of the corrosion for these alloys is reached, the effect of water vapour on the cation

diffusion and the role of nickel in low partial pressure of oxygen, e.g. steam condition, are still not clear. It becomes even more challenging because of very fine oxide structures obtained in the steam environment which cannot be identified properly by conventional analysis methods [44, 70-72]. In the screening and development of proper corrosion-resistant structural materials for the application in high-temperature environments, understanding the fundamental mechanisms that govern material corrosion is crucial.

Recent advances in high-resolution microscopy techniques, which allow for a more detailed characterization of material microstructure, have remarkably enhanced our understanding of a variety of previously unsolved phenomena [86-89]. Here, we undertake a fundamental study on the surface oxide scales grown on a Fe-21Cr-32Ni (type-800H alloy) high Cr-Ni austenitic steel and a Fe-17Cr-9Ni (type-304 steel) low Cr-Ni austenitic steel after exposure to high-temperature steam using characterisation techniques that span a number of length scales. The comprehensive micro-to-atomic scale observations made in the course of this study should shed light on the mechanisms controlling the superior corrosion resistance of high Cr-Ni austenitic steels at high temperatures.

2. Experimental

The materials used in this study are a Fe-21Cr-32Ni (type-800H alloy) and a Fe-17Cr-9Ni (type-304 steel) austenitic steels. Their chemical compositions are shown in Table 1. The average grain sizes of Fe-21Cr-32Ni steel and Fe-17Cr-9Ni steel were measured to be about 80 and 40 μm, respectively. Coupon specimens ($15 \times 10 \times 2$ mm^3) were machined from the as-received plate material that had been annealed at 1177 °C for 3 h in air followed by water quenching. The coupons were then ground and further polished up to a 1.0 μm finish, followed by 10 minutes of final treatment with colloidal silica. The colloidal silica was used to remove the cold-worked layer introduced by the prior mechanical polishing. The well-polished coupons were then exposed to the deaerated high-temperature steam at 600 °C in 25 MPa for 1500 h. The content of dissolved oxygen in the steam was controlled at lower than 10 ppb by bubbling high-purity Ar through the water. More details about the high-temperature testing can be found in [44, 70-72].

Table 1. Chemical compositions of Fe-21Cr-32Ni and Fe-17Cr-9Ni steels used in this study (wt. %)

Materials	Ni	Cr	Ti	Si	Mn	Al	P	S	Cu	C	Fe
Fe-21Cr-32Ni	31.6	20.51	0.52	0.15	0.57	0.53	0.012	0.001	0.4	0.07	Bal.
Fe-17Cr-9Ni	8.87	16.91	-	0.18	1.21	-	0.018	0.007	0.06	0.082	Bal.

In a Zeiss Merlin Scanning Electron Microscope (SEM) equipped with an Oxford Instruments Energy Dispersive X-ray (EDX) detector system, the microstructure and chemical composition of the surface oxide scale developed on 800H alloy were studied. In a dual beam Zeiss Crossbeam 540 Focused Ion Beam (FIB), site-specific Transmission Electron Microscope (TEM) thin foils were produced. A Zeiss Merlin SEM with an Optimus on-axis Transmission Kikuchi Diffraction (TKD) detector and an aberration-corrected JEOL ARM200F TEM with a Gatan Electron Energy Loss Spectroscopy (EELS) detector and an Oxford Instrument EDX detector were used to conduct higher resolution analyses on the TEM foils. Three-dimensional (3D) chemical composition analysis was conducted by Atom Probe Tomography (APT), using a LEAP 5000 XR.

3. Results

3.1 The oxidation of Fe-21Cr-32Ni steel

3.1.1 SEM/EDX analysis

The oxidized coupon of Fe-21Cr-32Ni steel was fine-polished to expose its cross-section. The thickness of the surface oxide scale was not uniform, ranging from 15 to 20 μm. Fig. 1a shows a typical morphology of the cross-section of the surface oxide scale. The surface oxide scale could be divided into two distinct layers based on the various contrasts seen in the SEM-InLens image: an outer oxide layer and an inner oxide layer. The interface between these two layers was very flat, which coincides with the original mirror-finished surface of the coupon prior to the autoclave testing. As a result, this interface is highlighted as the original specimen surface, by a white dashed line in Fig. 1a. The thickness of the outer oxide layer was generally uniform, about 10 μm. While the inner oxide layer was not uniform, with an average thickness of about 7 μm. Further examination indicates that the outer oxide layer included a high number of cavities. These cavities are pointed out by the blue dashed circles. The diameters of these cavities ranged from 500 nm to 3 μm. The cavities were also occasionally observed around the interface between the outer and inner oxide layers and in the metal matrix close to the oxide front. Compared with the outer oxide layer, the structure of the inner oxide layer appeared to be more compact, because far fewer cavities were observed in this layer, at least under the SEM characterization resolution.

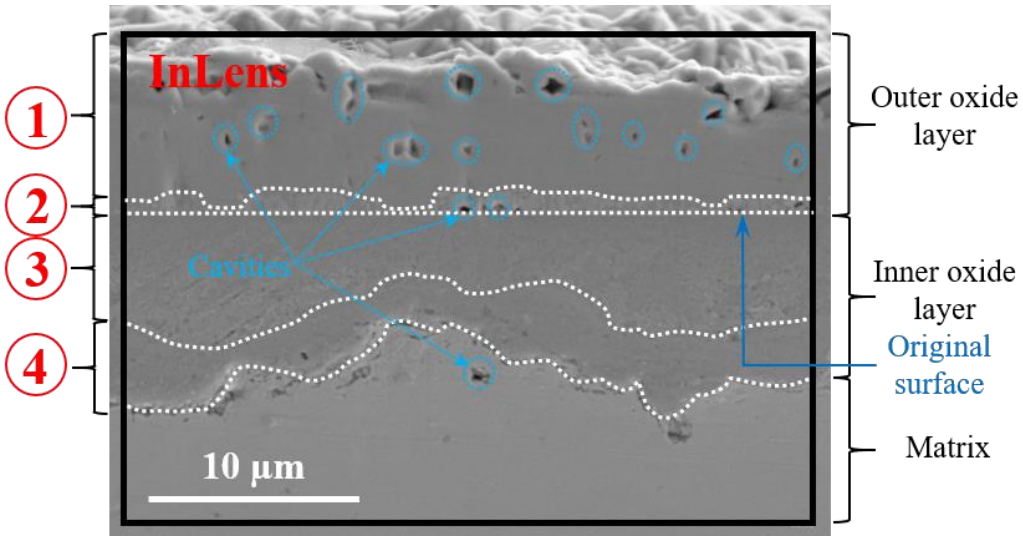

(a)

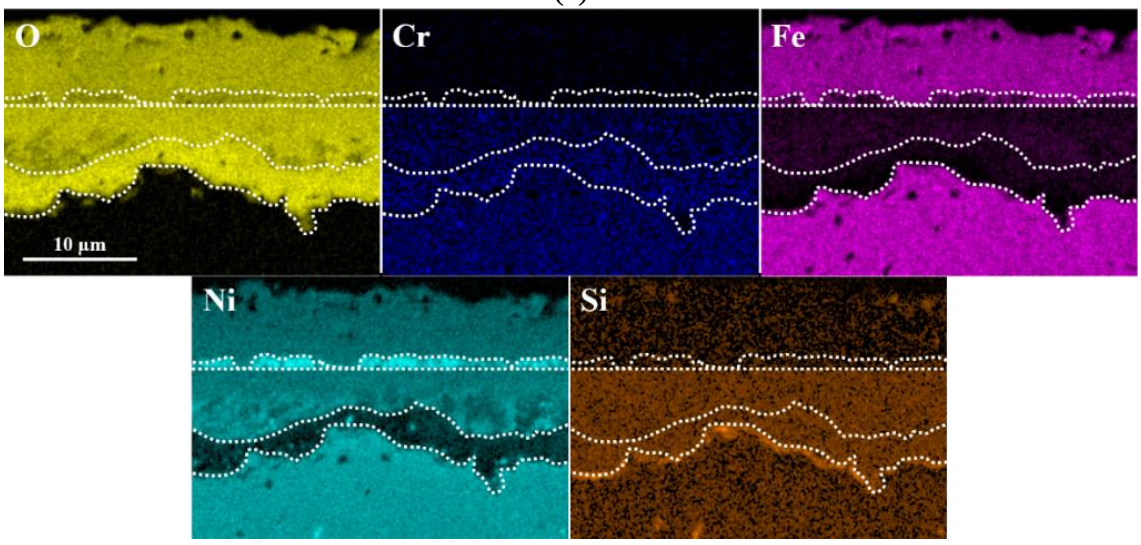

(b)

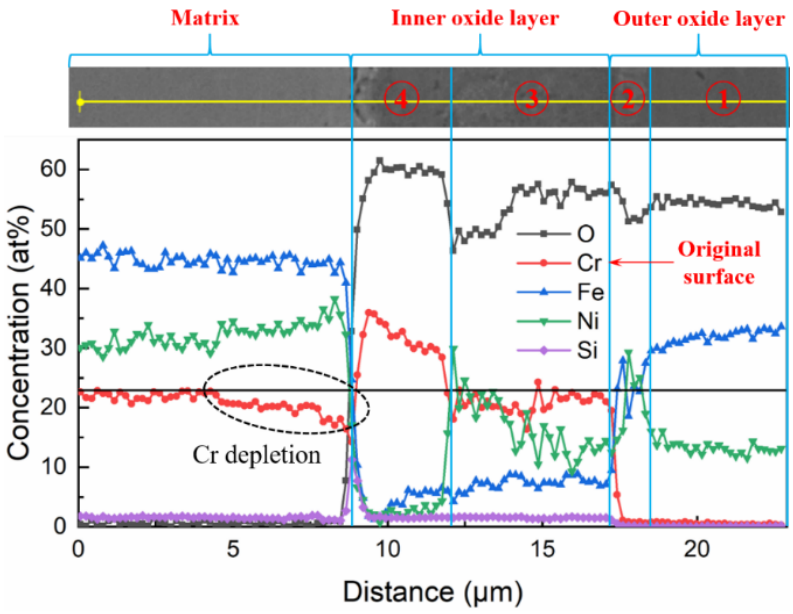

(c)

Fig. 1. (a) SEM-InLens image showing the cross-sectional morphology of the surface oxide scale formed on Fe-21Cr-32Ni steel; (b) SEM-EDX elemental maps showing the qualitative chemical composition distribution on the surface oxide scale cross-section; (c) SEM-EDX line profiles showing the quantitative chemical composition distribution across the surface oxide scale.

To examine the chemical composition distribution on the cross-section of the surface oxide scale, SEM-EDX mapping was conducted, as shown in Fig. 1b. It is seen that a rather high concentration of O was found in the two-layers of surface oxide scale. However, the distributions of other elements varied significantly in the oxide scale. The surface oxide scale can be further divided into four distinct layers, according to the distribution of Ni. The outer oxide layer can be divided into Layer-1 and Layer-2, and the inner oxide layer can be divided into Layer-3 and Layer-4. Layer-1 tended to be rich in O, Fe, and Ni, while Layer-2 mainly consisted of O, Ni, and some amount of Fe. All of the elements O, Cr, Fe, Ni, and Si existed in Layer-3, while Layer-4 appeared to be mainly composed of O and Cr. In addition, at the interface between Layer-4 and the metal matrix a thin semi-continuous Si-rich layer was found.

This four-layered structure was further confirmed by the SEM-EDX line-scanning across the cross-section of the surface oxide scale, as shown in Fig. 1c. The atomic ratios of O, Fe, and Ni in Layer-1 suggest that Layer-1 was highly likely to be mainly composed of $NiFe_2O_4$ spinel. The chemical compositions in Layer-2 and Layer-3 were complicated and the elemental atomic ratios in the two layers did not correspond to any well-known oxide species. Although the elemental atomic ratios in Layer-4 also did not correspond to any well-known oxide species, the content of Cr increased gradually towards the metal matrix, while Fe and Ni exhibited an opposite trend. Compared with other oxide layers, Layer-4 was mainly enriched in Cr. There was a Cr-depletion zone in the matrix, close to the oxide/matrix interface, highlighted by a black dashed circle in Fig. 1c.

3.1.2 TEM/EELS/EDX analysis

The results above reveal the existence of a 4-layered structure of the oxide scale. However, due to the lack of resolution of SEM, the detailed structure and chemical composition of these layers remain unclear. Hence, higher resolution analyses are required. Two site-specific TEM foils were prepared to examine the whole surface oxide scale. Fig. 2a shows the location of the two TEM foils in relation to

the cross-section of the surface oxide scale. The positions of the two site-specific TEM foils were selected in the purpose of covering the representative regions of the four different oxide layers. After FIB sample was thinned to a thickness of ~50 nm, the morphologies of the two TEM foils were preliminarily examined by SEM. The SEM-InLens and SEM-SE images of TEM samples 1 and 2 are shown in Figs. 2b and c, respectively. The four different oxide layers can still be identified by the different image contrasts, and the interfaces between different layers are highlighted by the black dashed lines.

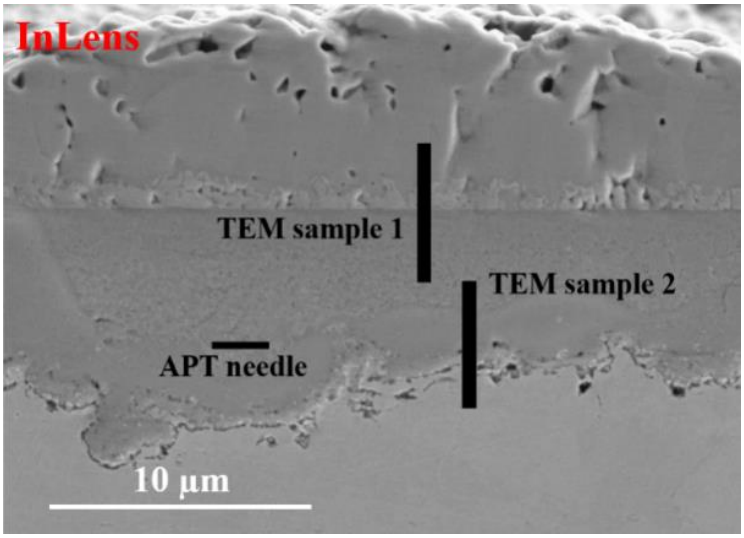

(a)

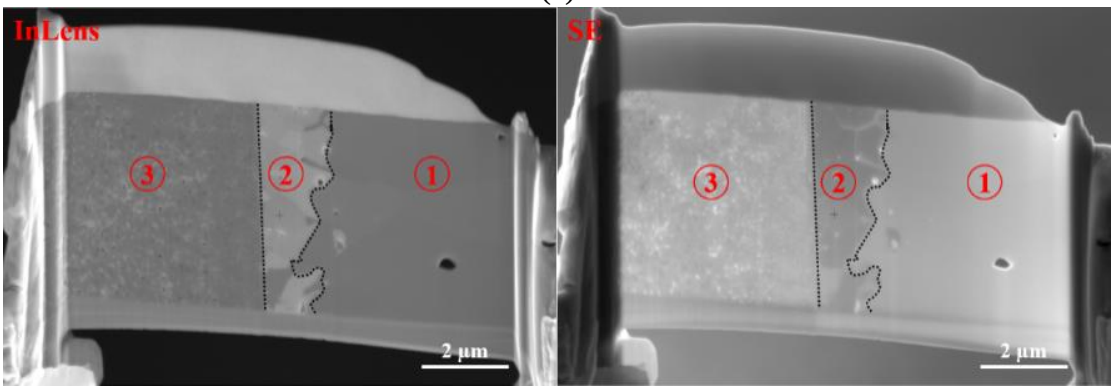

(b)

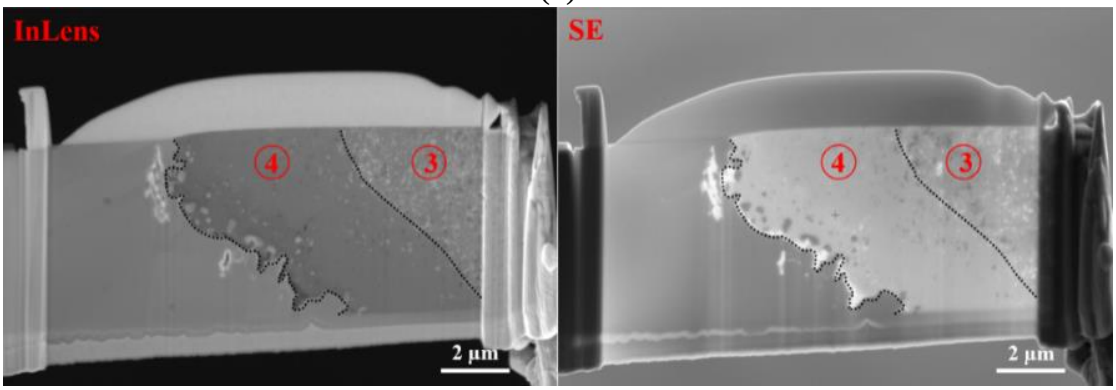

(c)

Fig. 2. (a) SEM-InLens image showing the positions of the two TEM foils prepared from Fe-21Cr-32Ni steel; (b) SEM-InLens and SEM-SE images showing the morphology of TEM sample 1; (c) SEM-InLens and SEM-SE images showing the morphology of TEM sample 2.

Under TEM imaging, different images can be obtained, depending on the collection angles of different detectors. In this study, high-angle annular dark-field (HAADF) and middle-angle annular dark-field (MAADF) images were collected simultaneously. The annular angular ranges used for the HAADF and MAADF imaging were 73–236 mrad and 33–51 mrad, respectively [90]. In the HAADF images, the image contrast was mainly produced by the different average atomic number and sample thickness, while MAADF images mostly exhibit diffraction contrast. The TEM samples prepared in this study had a generally uniform thickness, which has been proven by the thickness measurements of EELS low-loss spectrum. Hence, the image contrast in the HAADF images was mainly affected by the average atomic density. The morphology surrounding the interface between the metal matrix and Layer-4 is seen in the top-left HAADF image (Fig. 3). The oxide and metal matrix can be easily distinguished in the HAADF image because of their different atomic densities. The interface between the metal matrix and Layer-4 is highlighted by a white dashed line. It is seen that the image contrast in Layer-4 was not uniform. Some white particles or precipitates were observed. It suggests an ununiform chemical composition in this layer. The morphology around the original specimen surface is seen in the top-right HAADF image (Fig. 3). The positions of the original specimen surface and the interface between Layer-1 and Layer-2 are highlighted by the white dashed lines. The image contrasts in the three layers were different, suggesting that the oxide in these layers should have different chemical compositions. Compared with the HAADF imaging, the MAADF imaging was sensitive to the crystallographic orientations of the examined features. As shown in the bottom-left MAADF image, the different metal matrix grains can be identified by the MAADF image contrast. The oxide grains in Layer-1 and Layer-2 can also be distinguished by the MAADF image contrast (bottom-right image).

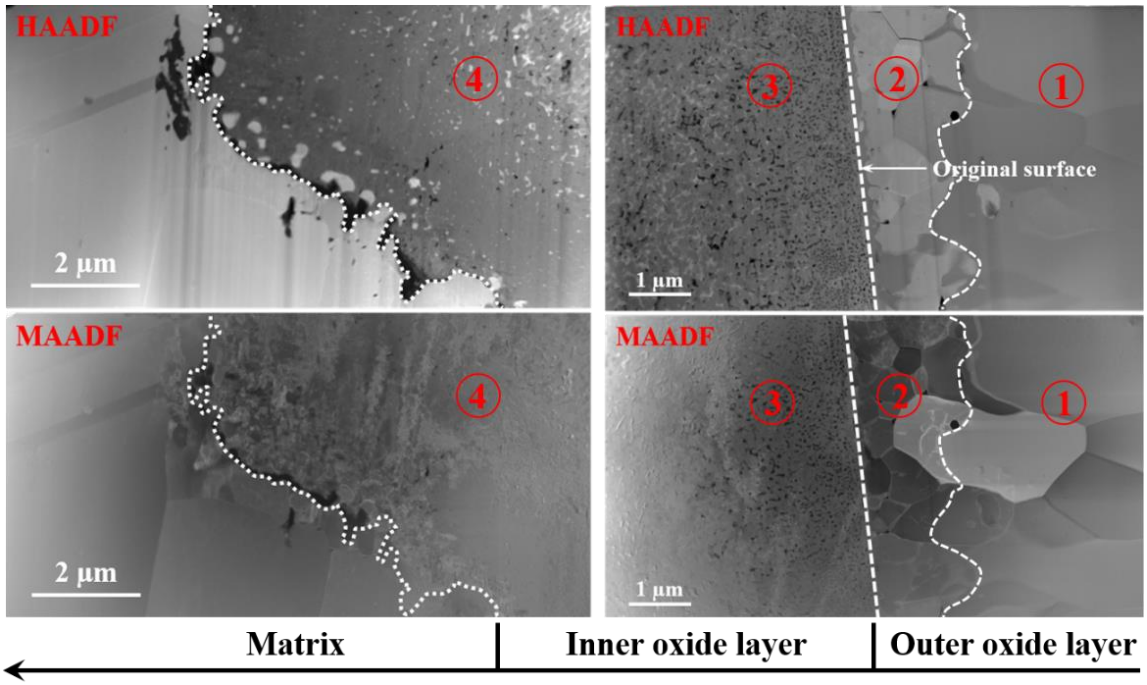

Fig. 3. Low-magnification HAADF and MAADF images showing the cross-sectional morphologies of the surface oxide scale formed on Fe-21Cr-32Ni steel. TEM sample 1: top and bottom right; TEM sample 2: top and bottom left.

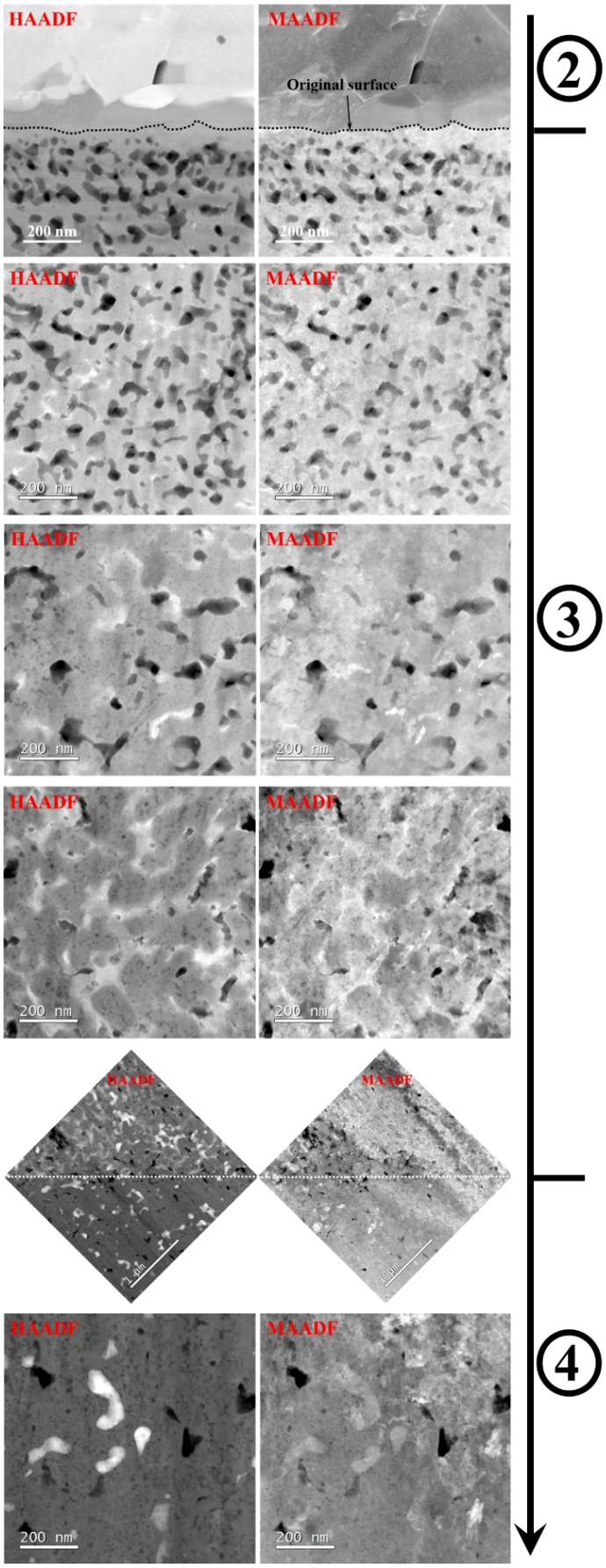

Fig. 4. HAADF and MAADF images showing the distribution of nano-pores in the surface oxide scale of Fe-21Cr-32Ni steel.

The HAADF images in Fig. 3 shows the existence of a large number of black spots in the inner oxide layer. The signal intensity in these spots was much lower than that in the other regions. These black spots were identified as nano-pores, ranging from 10 to 50 nm, which are believed to be formed during corrosion testing. As shown in Fig. 4, the nano-pores mainly existed in Layer-3, although they were also occasionally observed in Layer-4. In addition, the density of the nano-pores in Layer-4 decreased gradually in the direction towards to the inside of the material. The volume fractions of the nano-pores can be roughly estimated based on the image contrast in the HAADF images. The results show that the volume fractions of nano-pores in Layer-3 ranged from ~38% to ~5%. The structure of Layer-4 was much more compact than Layer-3, with a volume fraction of nano-pores lower than 3%.

Fig. 5a shows the representative HAADF morphologies of Layer-1, Layer-2, and Layer-3. The original specimen surface and the interface between Layer-1 and Layer-2 are pointed out by the red and blue dashed lines, respectively. The qualitative chemical composition maps in Fig. 5b show that Cr only existed in Layer-3 but not in Layer-1 or Layer-2. Both Ni and Fe were observed in Layer-1 and Layer-3, while only Ni was present in Layer-2. There was also a thin layer of oxide between Layer-2 and Layer-3. The thickness of this layer ranged from 100 to 200 nm. This layer was mainly composed of O and Fe. To quantify the chemical composition in these oxide layers, EELS line-scan was conducted (Fig. 5c). The atomic ratios of O, Cr, Fe, and Ni suggest that Layer-1, Layer-2, and Layer-3 were very likely composed of $NiFe_2O_4$, NiO, and $(Cr, Fe, Ni)_3O_4$ respectively. The accurate chemical composition atomic ratios in the thin layer, between Layer-2 and Layer-3, cannot be obtained because of significant overlap in the thickness direction. The representative background-subtracted EELS core-loss spectra extracted from Layer-1, Layer-2, and Layer-3 are shown in Fig. 5d, further confirming above composition analysis.

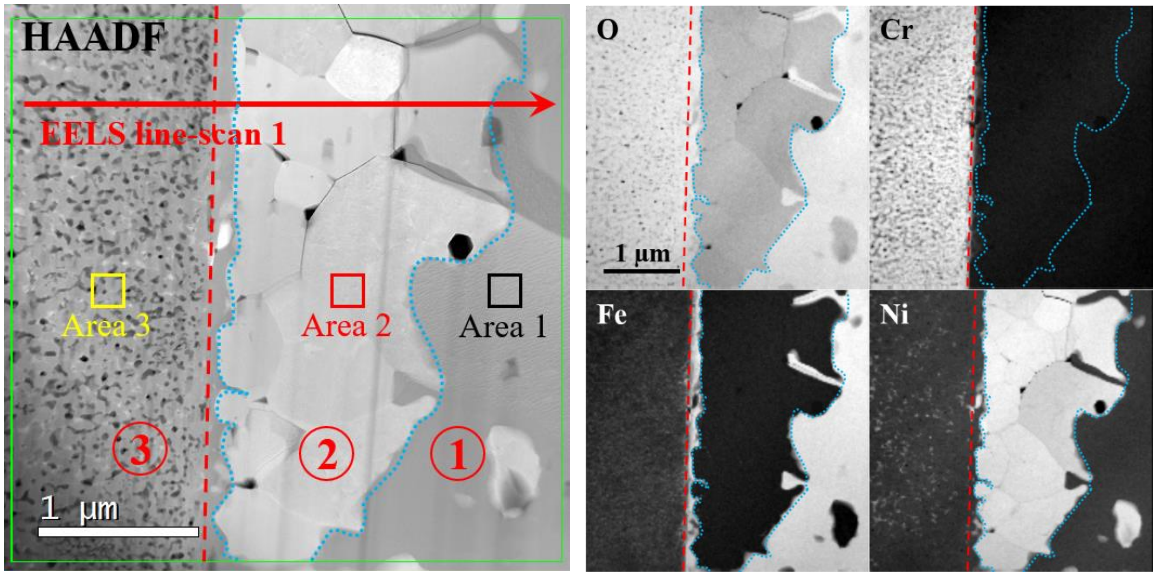

(a) (b)

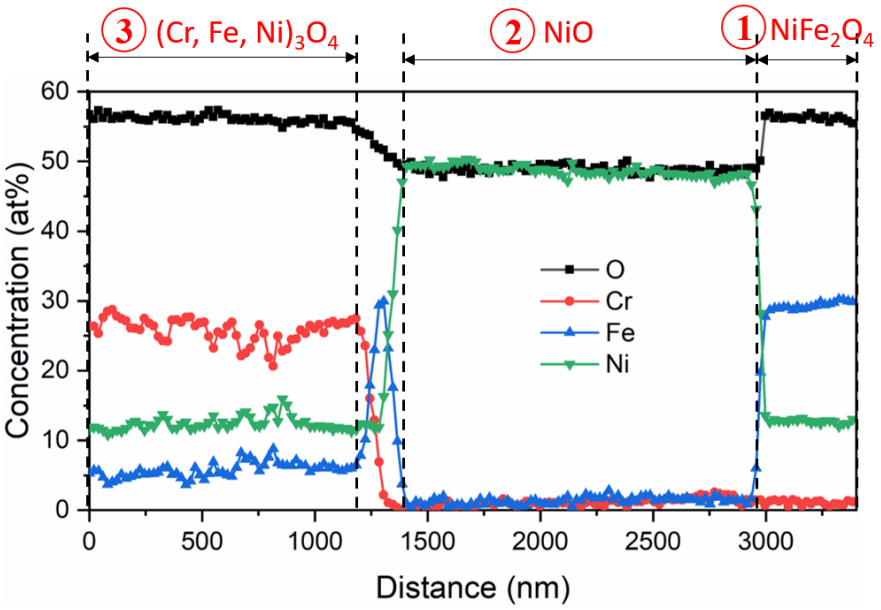

(c)

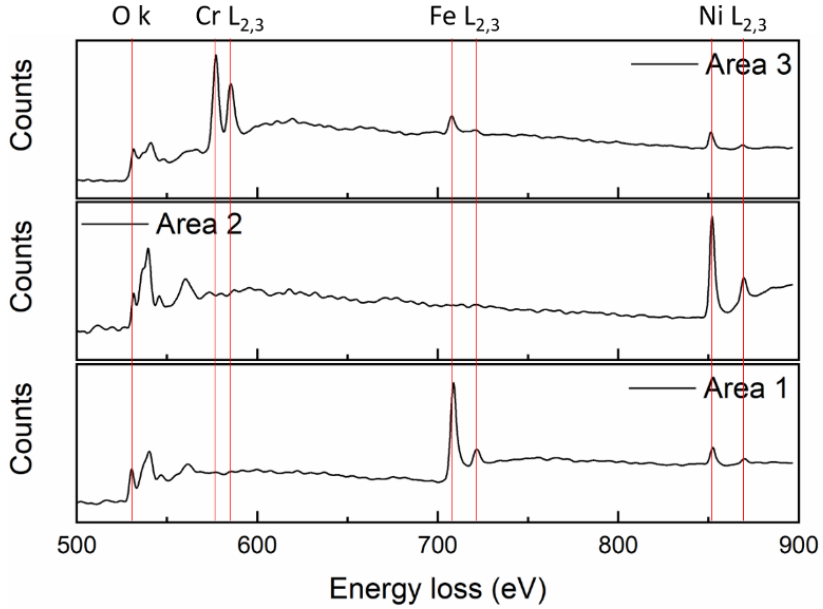

(d)

Fig. 5. Typical morphology and chemical composition of Layer-1, Layer-2, and Layer-3. (a) HAADF morphology and (b) qualitative EELS chemical composition maps showing the distribution of O, Cr, Fe, and Ni; (c) quantitative EELS chemical composition line-profiles showing the distribution of O, Cr, Fe, and Ni; (d) Background-subtracted EELS core-loss spectra extracted from Area 1, Area 2, and Area 3.

The HAADF image in Fig. 6a shows the morphology around the interface between Layer-3 and Layer-4. The interface is highlighted by the red dashed line. Fig. 6b shows the EELS chemical composition distribution in the two layers. It is seen that the two layers appeared to have similar chemical composition, being mainly composed of O, Cr, and Fe. Ni also existed in the two layers, but the content of Ni in Layer-3 was much higher than in Layer-4, which corresponds well with the results in Fig. 1c. In addition, the distribution of Ni in the two layers was not uniform. Ni-rich networks were observed in Layer-3, while only a few isolated Ni-rich particles existed in Layer-4. Fig. 6c shows a quantitative EELS line-scan. The atomic ratios show that the regions without Ni-rich networks in Layer-3 were

very likely to be composed of (Cr, Fe, Ni)$_3$O$_4$. However, compared with Layer-3, the content of Ni in Layer-4 (Ni-rich particle free region) was much lower, which is supposed to be mainly composed of (Cr, Fe)$_3$O$_4$. The chemical composition measured from the Ni-rich particles/networks did not correspond to any well-known species, which might be due to the overlap of more than one phase in the thickness direction. Five background-subtracted EELS core-loss spectra were extracted from the two layers, as shown in Fig. 6d. O, Cr, Fe, and Ni peaks were observed in Area 4, while Ni peaks were not observed in Area 7. The only observation of O and Ni peaks in Area 6 suggests the existence of NiO. The core-loss spectra from Area 5 and Area 8 only show Ni peaks, indicating that metallic Ni also existed in these regions. These results suggest that the abnormal chemical composition measured from Ni-rich particles/networks in Fig. 6c might be due to the overlap of metallic Ni, NiO, (Cr, Fe)$_3$O$_4$, and (Cr, Fe, Ni)$_3$O$_4$. The chemical composition of the Ni-rich particles/networks was further examined by 3D APT to overcome the potential overlap issue, which will be shown later.

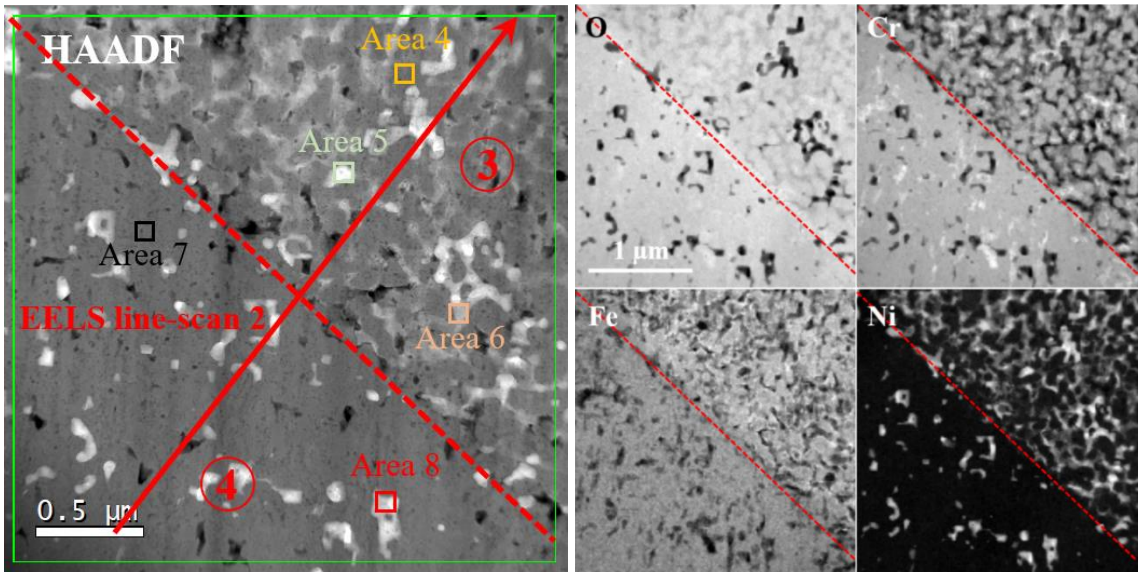

(a) (b)

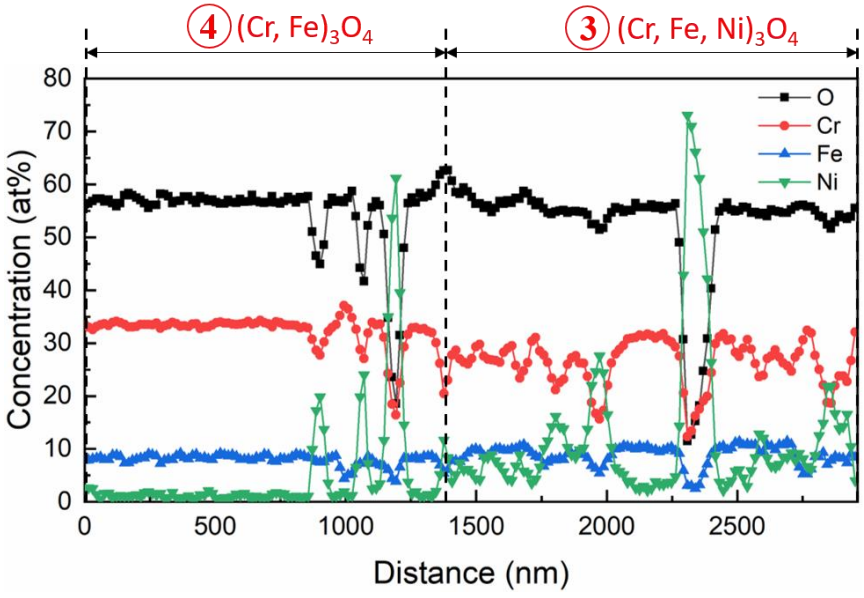

(c)

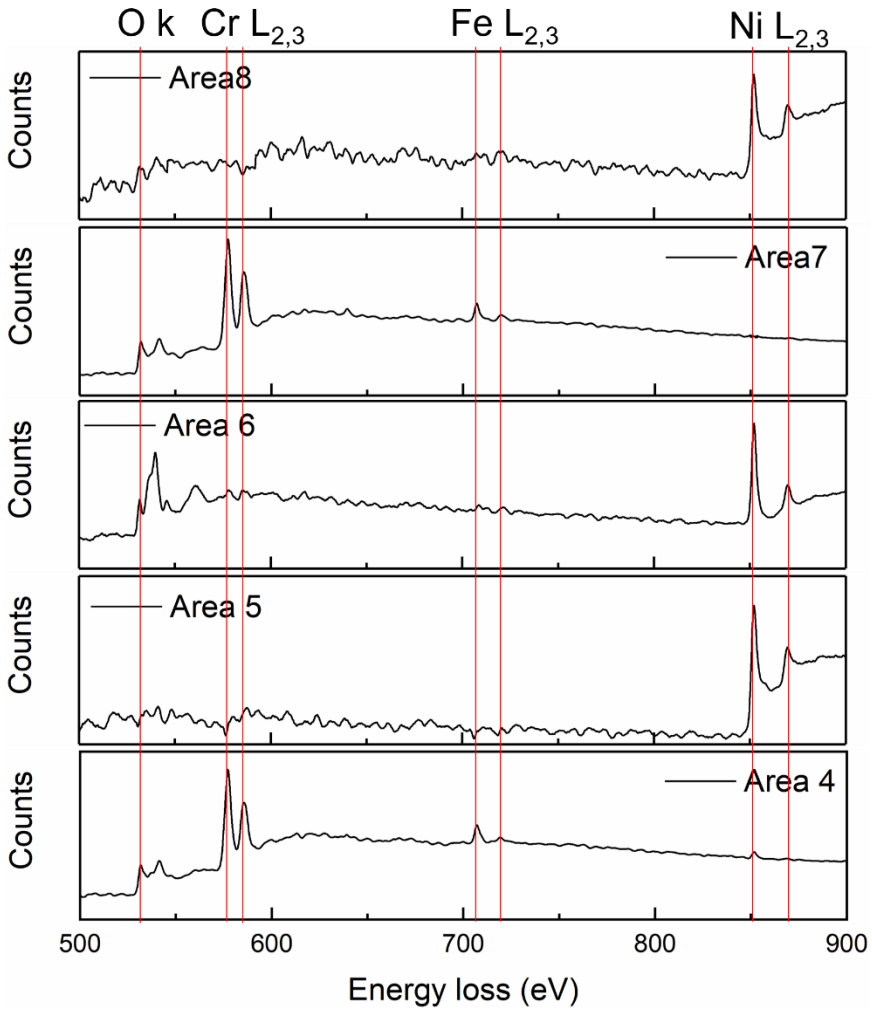

(d)

Fig. 6. Typical morphology and chemical composition in Layer-3 and Layer-4. (a) HAADF morphology and (b) qualitative EELS chemical composition maps showing the distribution of O, Cr, Fe, and Ni; (c) quantitative EELS chemical composition line-profiles showing the distribution of O, Cr, Fe, and Ni; (d) Background-subtracted EELS core-loss spectra extracted from Area 4, Area 5, Area 6, and Area 7.

Fig. 7a shows the HAADF morphology around the oxidation front. The oxide-metal matrix interface is highlighted by the red dashed line. The EELS chemical composition maps in Fig. 7b show that apart from the Ni-rich particles, the chemical composition in the oxide was also not uniform. There was a thin continuous layer of oxide with a thickness of 1-2 µm at the front of Layer-4 which is labelled as Layer-5. This layer was mainly composed of Cr and O, which is different from Layer-4, where O, Cr, and Fe were present. Further observation shows that there was a semi-continuous layer between Layer-5 and the metal matrix. This sublayer is labelled as Layer-6. The interface between Layer-6 and Layer-5 is highlighted by blue dashed lines. Only O was observed in this semi-continuous layer. This might be because the other components in this layer are out of the examined range of EELS energy loss (450-950 eV) in this study. The atomic ratios obtained from EELS line-scan in Fig. 7c suggest that Layer-4 and Layer-5 were very likely to be mainly composed of $(Cr, Fe)_3O_4$ and Cr_2O_3, respectively. The representative background-subtracted EELS core-loss spectra extracted from Layer-4, Layer-5, and the metal matrix are shown in Fig. 7d.

As mentioned above, the chemical composition of Layer-6 cannot be obtained from EELS. Hence, EDX mapping was conducted. Fig. 8a shows the HAADF image, while the related EDX chemical composition maps are shown in Fig. 8b. It can be seen that Layer-6 was mainly composed of Si and O. The K edge energy of Si is 1839 eV, which is outside the examined EELS energy range (450-950 eV) in this study. This explains why Si was not observed by EELS. The chemical composition at Area 12 was measured by EDX, and was observed to be 30% O, 65% Si, 3% Cr, and 2% Fe (at. %). The results suggest that the oxide in Layer-6 was very likely to be mainly composed of SiO_2. It is worth noting that several Al-rich oxide particles existed in the metal matrix near Layer-6.

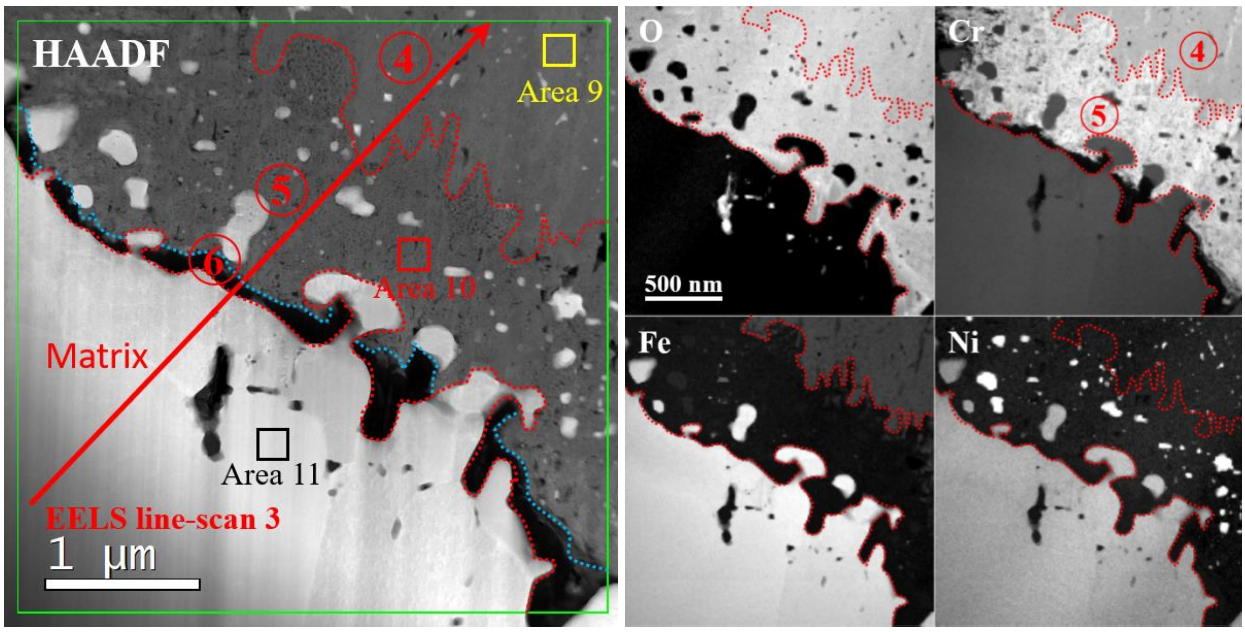

(a) (b)

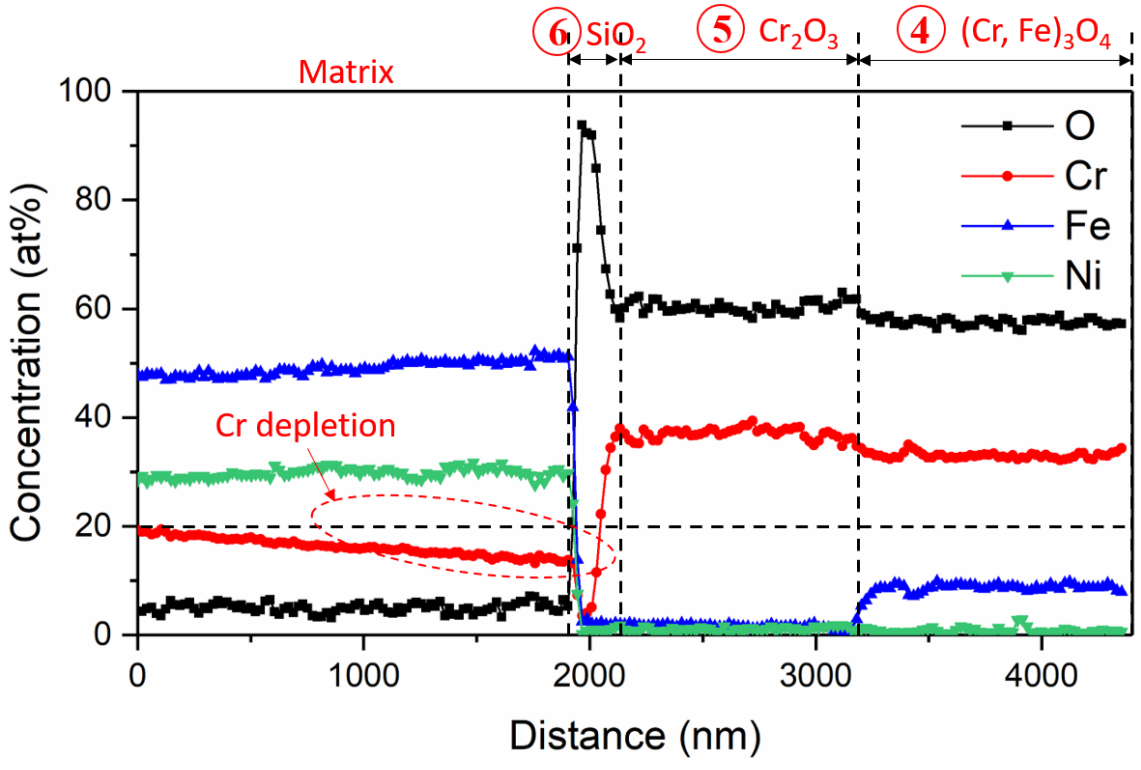

(c)

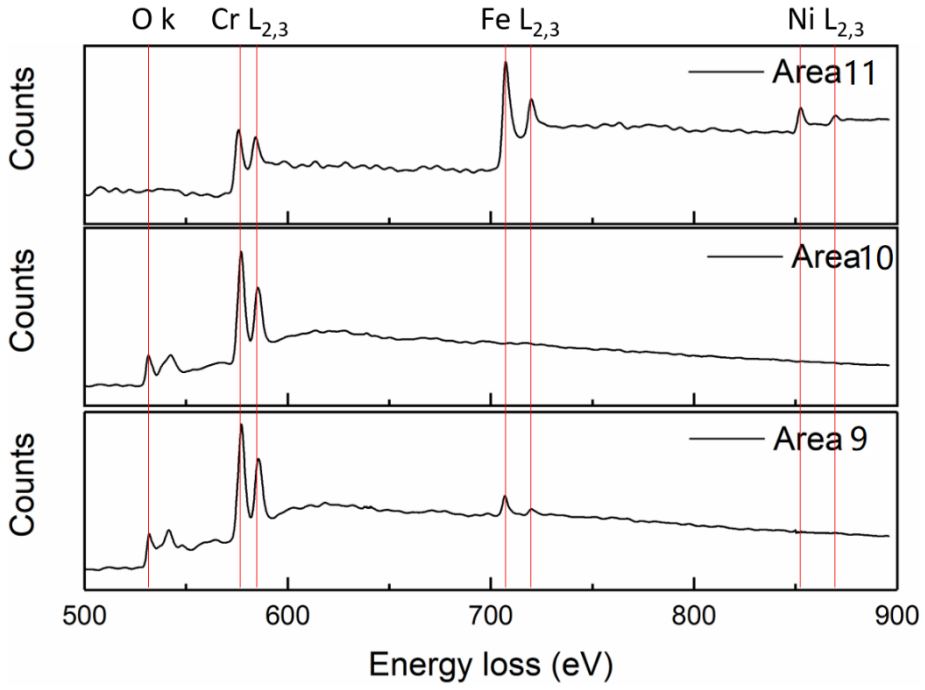

(d)

Fig. 7. Typical morphology and chemical composition in Layer-4, Layer-5, and Layer-6. (a) HAADF morphology and (b) qualitative EELS chemical composition maps showing the distribution of O, Cr, Fe, and Ni; (c) quantitative EELS chemical composition line-profiles showing the distribution of O, Cr, Fe, and Ni; (d) Background-subtracted EELS core-loss spectra extracted from Area 9, Area 10, and Area 11.

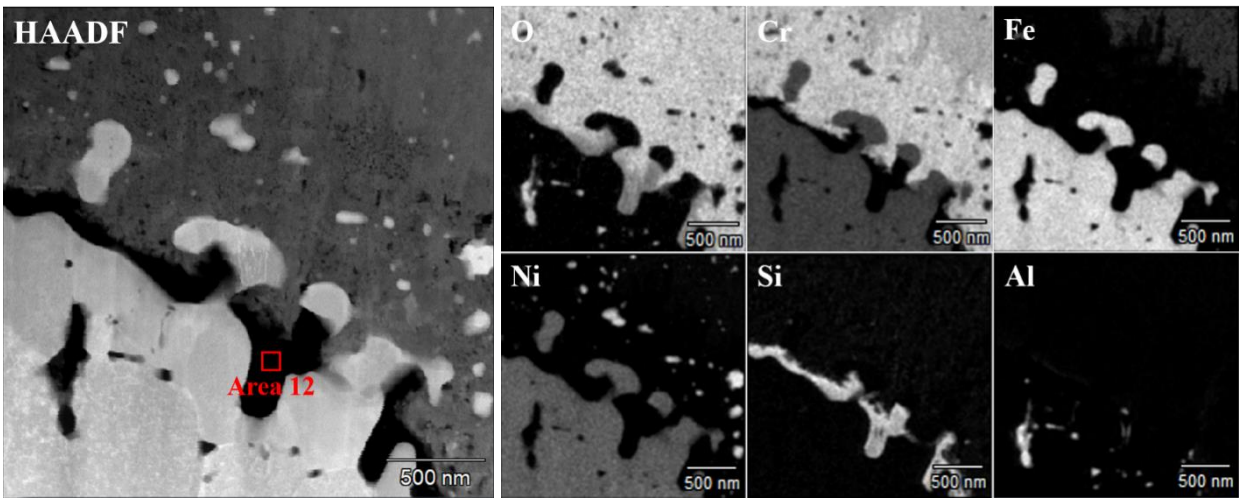

(a) (b)

Fig. 8. Typical morphology and chemical composition in Layer-4, Layer-5, and Layer-6. (a) HAADF morphology and (b) qualitative EDX chemical composition maps showing the distribution of O, Cr, Fe, and Ni.

3.1.3 APT analysis

As shown in Fig. 6, the overlap between the oxide and the Ni-rich particles/networks in Layer-3 prevents the accurate measurement of the chemical composition of these Ni-rich phases via EELS. To overcome the overlap issue caused by TEM, a 3D characterization technique with high spatial and chemical resolution, APT, was applied. The APT samples used in this study were prepared from Layer-

3, close to the interface between Layer-3 and Layer-4, as shown in Fig. 2a. Although 8 samples were prepared, 7 of them fractured during the APT testing before useful data were collected. Only one needle was successfully analyzed, and more than 20 million ions were collected. Fig. 9a shows the spatial separation of the oxide and the Ni-rich phase (O in red, Cr in pink, Fe in blue, and Ni in cyan). To qualitatively show the elemental distribution in the two phases, the 3D APT data set was used to extract a region of interest with a thickness of 5 nm. It is seen that the oxide mainly consisted of O, Cr, Fe, and Ni, and that the Ni-rich precipitate appeared to be mainly composed of Ni (Fig. 9b). Fig. 9c shows a line-scan across the interface of the two phases to quantify the elemental distribution. The atomic ratios suggest that the oxide and the Ni-rich phase were very likely to be $(Cr, Fe, Ni)_3O_4$ and metallic Ni precipitate, respectively. These results correspond well with the results obtained from EELS (Fig. 6).

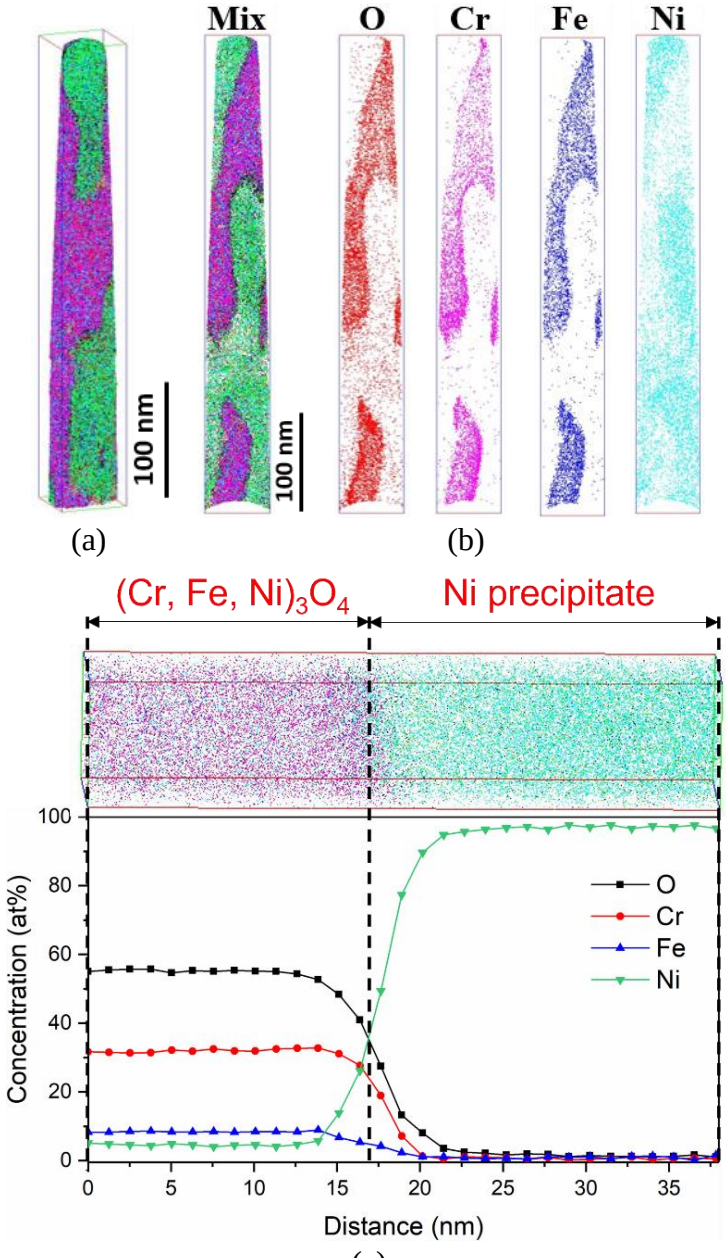

Fig. 9. (a) APT data set showing the 3D distribution of the oxide and Ni precipitate; (b) spatial distribution of O, Cr, Fe, and Ni in separate data sets; (c) concentration profiles across the oxide-Ni precipitate interface.

3.1.4 TKD analysis

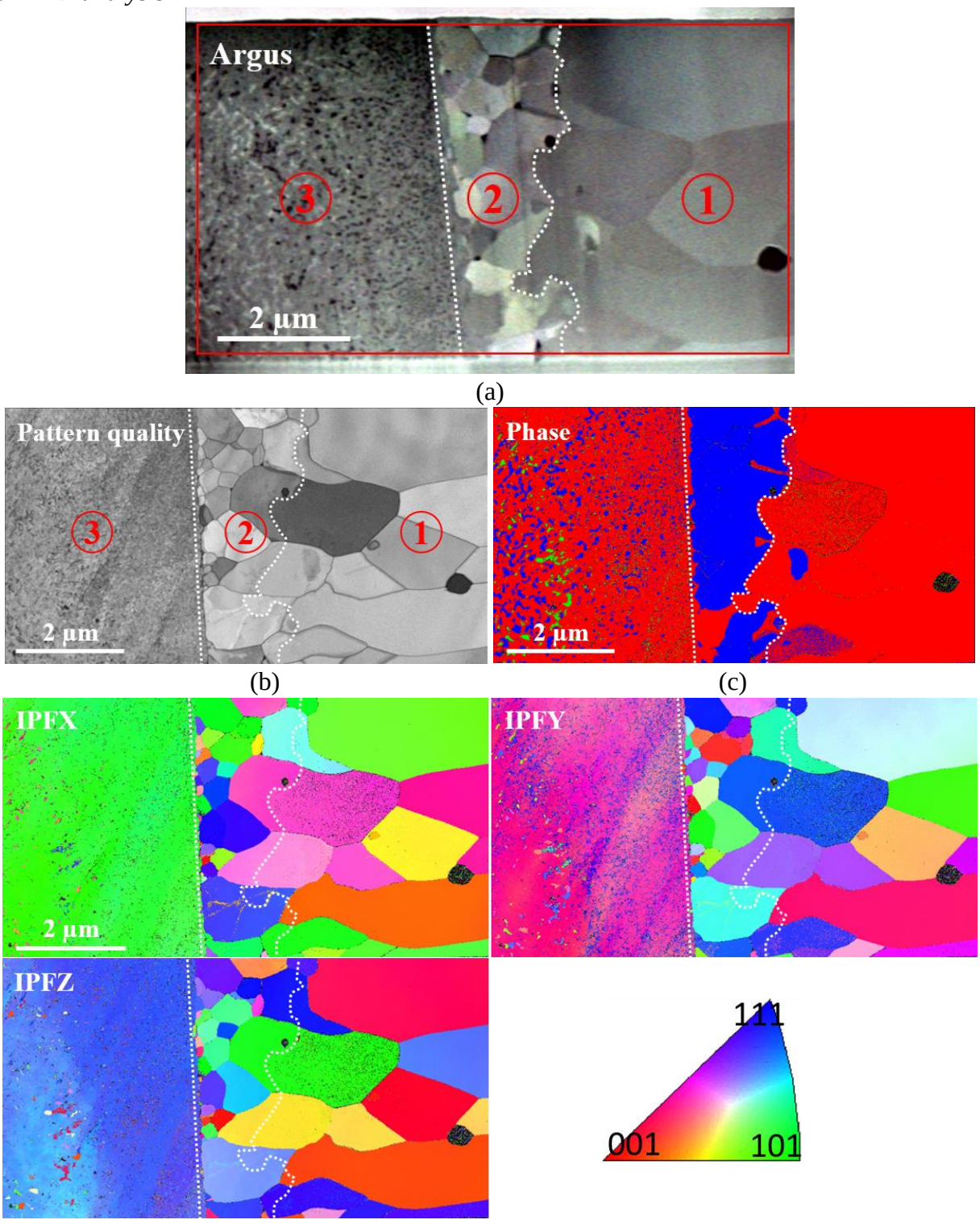

Fig. 10. TKD analysis on TEM sample 1 (step size=3 nm, collected Kikuchi pattern resolution=800 × 1200). (a) Argus map; (b) pattern quality map; (c) phase map; (d) IPF maps with orientation legend.

TEM foil 1 in Fig. 2 was analysed by TKD. Fig. 10a shows the Argus map collected by the Bruker EBSD detector. The nano-pores in Layer-3 and the oxide crystal morphologies in Layer-1 and Layer-2 can all be observed in this image. The TKD pattern quality map is shown in Fig. 10b, in which the

oxide grains in Layer-1 and Layer-2 can be more easily observed. Fig. 10c shows the TKD phase map, in which the Ni/NiO, spinel, and Cr_2O_3 are shown in blue, red, and green, respectively. Since metallic Ni and NiO have very similar crystallographic structure, they cannot be distinguished under TKD. This is why they appeared in the same colour in the TKD phase map. It is seen that Layer-2 was mainly indexed as NiO, which is consistent with the results shown in Fig. 5. It is worth noting that (Cr, Fe, Ni)$_3O_4$ and $NiFe_2O_4$ all belong to the group classified as spinel and have very similar crystallographic structures. These very similar structures also cannot be distinguished by TKD. Hence, although the chemical composition in Layer-1 and Layer-3 was different, they were all indexed as spinel. Apart from spinel, Ni/NiO and Cr_2O_3 were also observed in Layer-3. Although the interface between Layer-1 and Layer-2 can be easily identified, based on their different chemical compositions, it is difficult to identify the interface on the Inverse Pole Figure (IPF) images, because the different oxides in the two layers co-existed in the same grains, as shown in Fig. 10d. The spinel oxides in Layer-3 belonged to a same grain. The Ni/NiO precipitates in Layer-3 had the same crystallographic orientation with the surrounding spinel oxides. The crystallographic orientations of the Cr_2O_3 precipitates in Layer-3 were different from the surrounding spinel oxides.

(a)

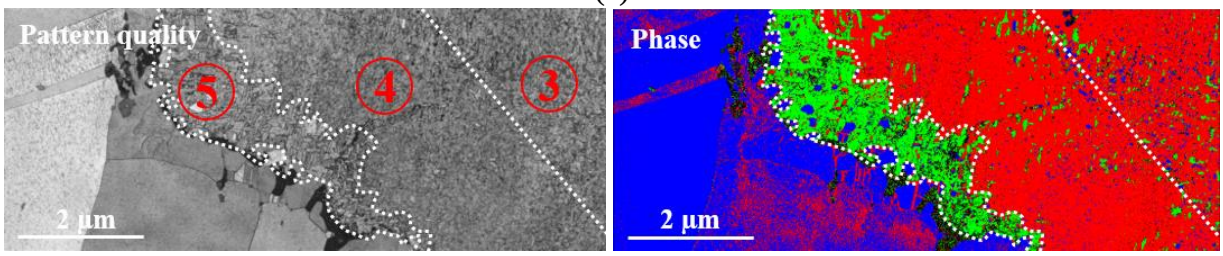

(b) (c)

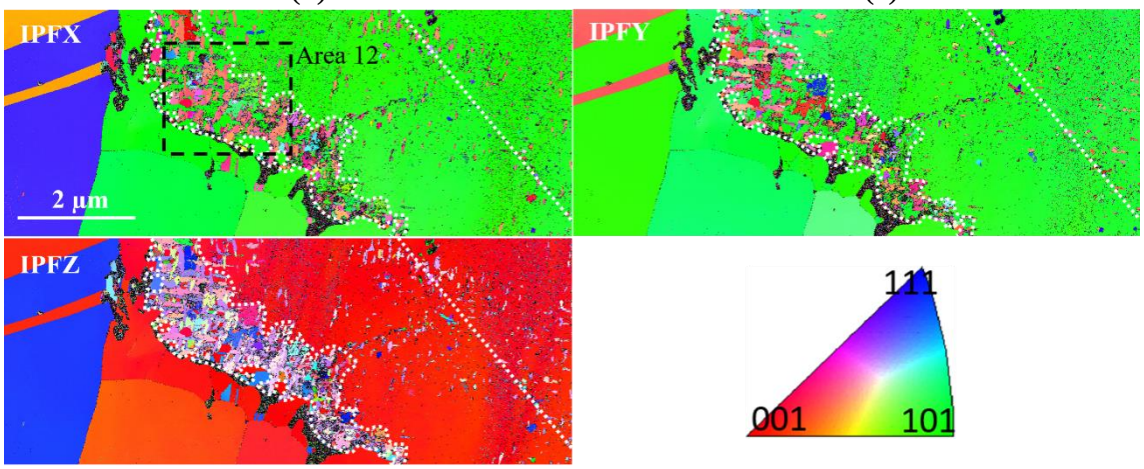

(d)

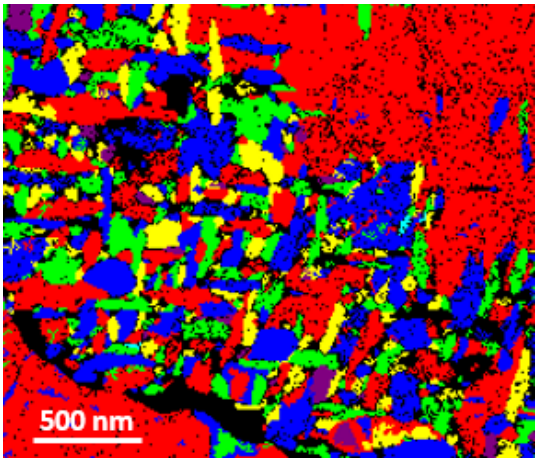

(e)

Fig. 11. TKD analysis on TEM sample 1 (step size=3 nm, collected Kikuchi pattern resolution=800 × 1200). (a) Argus map; (b) pattern quality map; (c) phase map; (d) IPF maps with orientation legend; (e) enlarged grain shape image in Area 12.

TEM foil 2 in Fig. 2 was also analysed by TKD. Layer-3, Layer-4, and Layer-5 can be distinguished in the Argus map due to the different image contrasts (Fig. 11a). The semi-continuous Layer-6 can also be observed, but the interfaces of this layer are not highlighted in this image. Fig. 11b shows the pattern quality map. Apart from Layer-6, the other regions had been well indexed. Fig. 11c shows the phase map, in which the austenite metal, spinel, and Cr_2O_3 were shown in blue, red, and green, respectively. It is seen that Layer-3 and Layer-4 were mainly composed of spinel oxides, although Cr_2O_3 and metallic Ni precipitates were also observed in the two layers. Layer-5 is mainly indexed as Cr_2O_3. The white particles in this layer (Fig. 11a) are identified as austenite metal. The IPF images in Fig. 11d show that the oxides in Layer-3 and Layer-4 belonged to a same grain. Although the oxides in the two layers were different (Fig. 6), they are all identified as spinel. Further observation shows that the oxides in Layer-3 and Layer-4 had the same crystallographic orientations with the underneath unoxidized metal grain. In addition, the austenite metal particles in the two layers also retained the same crystallographic information with the underneath metal grain. Compared with the oxides in Layer-3 and Layer-4, the oxides in Layer-5 consisted of nano-sized multi-crystalline Cr_2O_3. The nano-sized grains appeared to have random crystallographic orientations. Further observation shows that the nano-sized grains were neither equiaxed nor columnar, with some grains elongated along some specific orientations, as shown in Fig. 11e. The chemical composition analysis showed that the oxides in Layer-6 were very likely to be SiO_2 (Fig. 8), while they were not well indexed by TKD.

It is worth noting that the red pixels in the metal matrix beneath the Cr_2O_3 layer (Fig. 11c) are the artifact caused by TKD instead of spinel. This is because the austenite and spinel have a similar crystallographic structure and mis-indexing may occur occasionally. Similar phenomenon was also reported in [91].

3.1.5 Early-stage oxidation in high-temperature steam

To understand the formation of a NiO layer on the specimen surface (Figs. 5 and 10), an early-stage (48 h) oxidation test in the same high-temperature steam environment was conducted. Fig. S1a shows the SEM and HAADF cross-sectional morphology of the surface oxide scale. It can be seen that the morphology of the early-stage oxide scale was very different from that oxidized for 1500 h. A layer of co-existing oxide and metal was observed, which indicates the occurrence of internal oxidation [5].

The volume fraction of the internal oxide was ~50%. In addition, there was a metallic Ni layer just above the internal oxide layer. This metallic Ni above the internal oxide layer had been reported by many researchers [92-95]. Further observation shows an outermost oxide layer just above the metallic Ni layer. The atomic ratios measured by EELS show that the oxides in the internal oxide layer (30% Cr, 15% Fe, 55% O) and the outermost layer (52% Ni, 46% O, 4% Fe) were very likely to be composed of $(Cr, Fe)_3O_4$ and NiO, respectively. The representative background-subtracted EELS core-loss spectra extracted from Area 13, Area 14, Area 15, Area 16, and Area 17 are shown in Fig. S1b. The co-existence of oxide and metal phases in the inner oxide layer was also observed in 800H alloy after exposure to 650 °C high-temperature steam for 250 h [96].

3.2 The oxidation of Fe-17Cr-9Ni steel

The SEM morphology of the cross-section of Fe-17Cr-9Ni steel after oxidized in 600 °C high-temperature steam for 1500 h is shown in Fig. 12a. The surface oxide scale appeared to have a duplex structure. The thicknesses of the inner and outer oxide layers were ~70 and ~50 μm, respectively. The SEM-EDX/EBSD analysis on the cross-section of the surface oxide scale has been reported in [70]. The outer oxide layer was composed of columnar magnetite. Three TEM samples were prepared to examine the microstructure and microchemistry of the inner oxide layer. The positions of the three TEM samples are shown in Fig. 12a. The nano-to-atomic scale characterization on TEM samples 4 and 5 had been conducted in [70]. Although the inner oxide layer appeared to be continuous under the microscale characterization, it was revealed to be composed of oxide and metal phases under nano-to-atomic scale characterization, which is a typical feature of an internal oxidation zone (IOZ). The TEM sample 3 was not examined in [70], and its SEM morphology is shown in Fig. 12b. The inner oxide layer around the outer-inner oxide layer interface was very porous. The HAADF image obtained from the Region 1 in Fig. 12b confirmed the existence of a large number of nano-pores in the inner oxide layer, ranging from 10 to 50 nm, which is very similar to that observed in Fe-21Cr-32Ni steel (Fig. 4). The representative HAADF morphology of the inner oxide layer from the outer-inner oxide layer interface to the inner oxide layer-matrix interface is shown in Fig. 13. It is seen that the morphology of the inner oxide layer near the outer-inner oxide layer interface was very different from that near the inner oxide layer-matrix interface. The volume fraction of the metal phase in the inner oxide layer gradually increased towards the metal matrix. However, the volume fraction of the nano-pores exhibited an opposite trend. Compared with the nano-pores in the region near the outer-inner oxide layer interface, the size of the nano-pores in the region near the inner oxide layer-matrix interface was much smaller, only 1-5 nm [70].

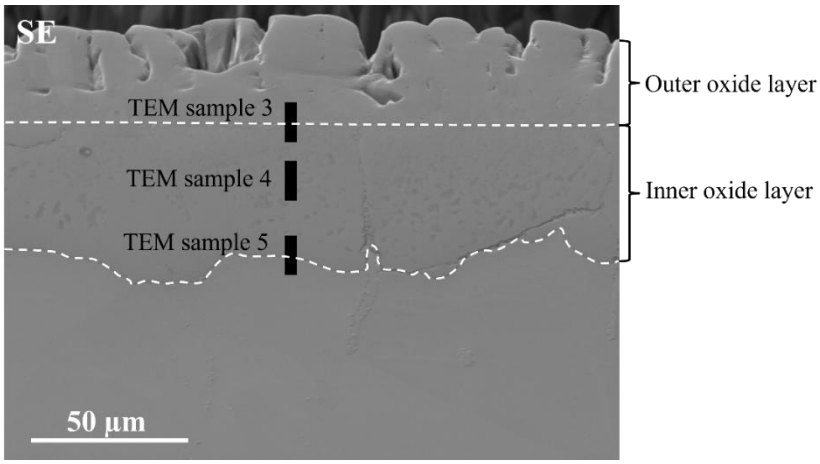

(a)

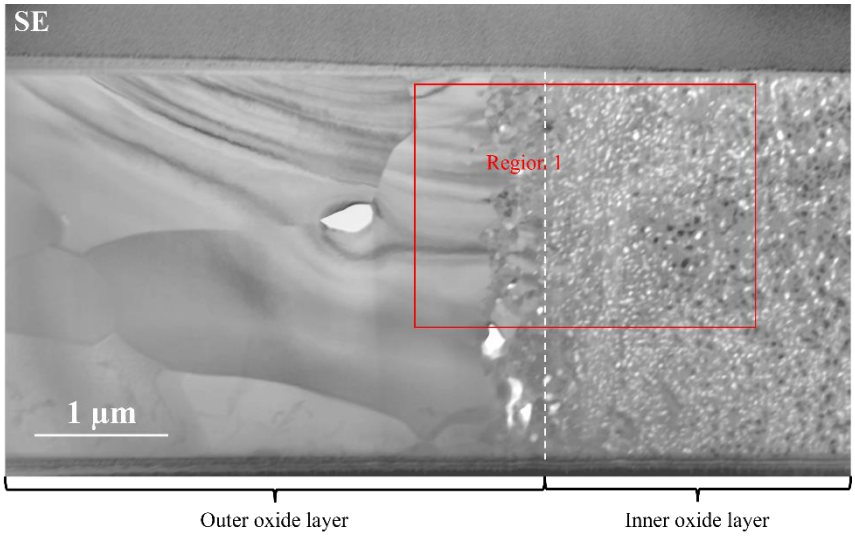

(b)

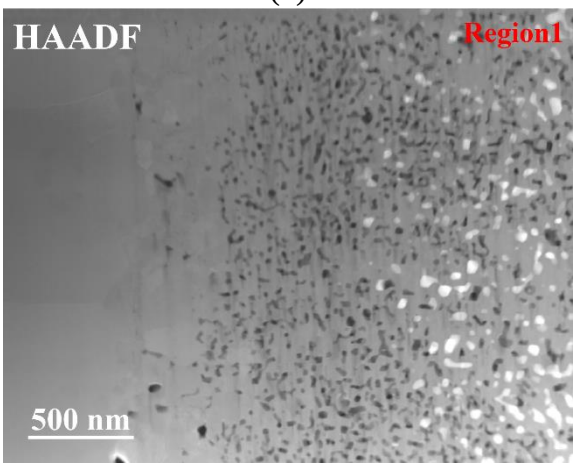

(c)

Fig. 12. (a) SEM-SE image showing the positions of the three TEM foils prepared from Fe-17Cr-9Ni steel; (b) SEM-SE image showing the morphology of TEM sample 3; (c) HAADF image showing the morphology of Region 1 in (b).

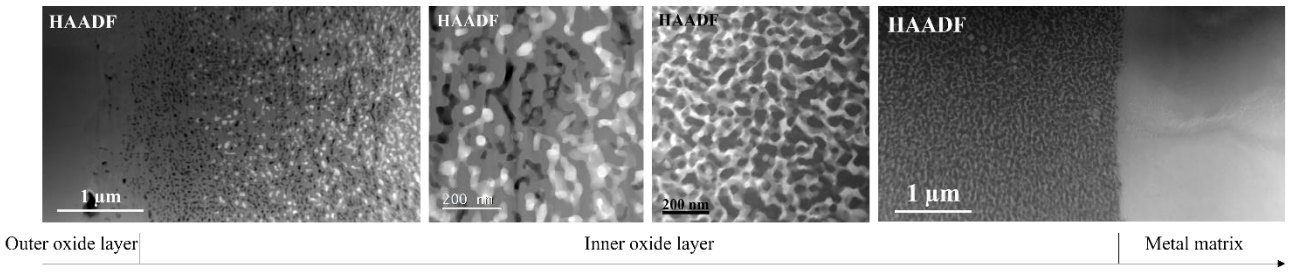

Fig. 13. Representative HAADF images showing the morphology of the inner oxide layer of Fe-17Cr-9Ni steel.

4. Discussion

In this study, Fe-21Cr-32Ni and Fe-17Cr-9Ni steels were oxidized in 600 °C high-temperature steam for 1500h. The microstructure and microchemistry of the surface oxide scales of the two steels have been studied and compared by multi-techniques. Since the surface oxide scale of Fe-17Cr-9Ni steel has been studied in detail in [70], this study is mainly focus on Fe-21Cr-32Ni steel. Based on the results presented above and in literature, the microprocesses of corrosion product formation in correlation

with the mass transfer and the effect of alloy composition on corrosion in the high-temperature steam condition are discussed below.

4.1 Thermodynamics in the high-temperature steam environment

The equilibrium oxygen partial pressure in 25 MPa steam at 600 °C was calculated to be ~2.7×10^{-7} atm by using FactSage [97]. According to the equilibrium phase fraction, as a function of oxygen partial pressure for a ternary Fe-Cr-Ni steel reported in [75], Cr_2O_3, (Cr, Fe, Ni)$_3O_4$, NiO are predicted to form on the alloy. This prediction is consistent with the experimental results obtained in this study. However, it does not explain the experimentally observed distribution of the different oxide species in the oxide scale. Thermodynamic calculations conducted in [75] were based on an assumption of a constant alloy composition and a constant oxygen partial pressure during the oxidation process. However, in a practical situation, neither the alloy composition, nor the oxygen partial pressure is constant. The different diffusivities of the alloying elements will change the alloy composition locally, and so the partial pressure of oxygen in the oxide layers. A discussion on mass transfer based on the experimental data obtained in this work is necessary since the thermodynamic calculation alone cannot adequately explain the formation of the multi-layered surface oxide scales.

4.2 The early-stage oxidation of Fe-21Cr-32Ni steel in high-temperature steam

Fig. S1 shows that Fe-21Cr-32Ni steel was initially oxidized by the inward diffusion of oxygen to form dispersed (Cr, Fe)$_3O_4$ spinel in the high-temperature steam environment. The internal oxide formation is determined by the oxygen inward diffusion and the cation outward diffusion. It is generally believed that the presence of water vapour could accelerate oxygen inward diffusion [17, 98, 99] and initiate internal oxidation. The nucleation of internal oxides occurs preferentially in the region where Cr is enriched because of a much lower oxygen potential required for Cr-rich oxide formation, e.g. Cr_2O_3 or (Cr, Fe)$_3O_4$ depending on local pO_2 [4, 5]. The growth of these nuclei would accelerate Cr and Fe diffusion towards the oxides but expel Ni to the surrounding metal, leading to the formation of a Ni enriched matrix around the internal oxides (Fig. S1). Since the Pilling-Bedworth ratio of the internal oxide precipitates (spinel) was reported to be around 2.0 [100], the growth of the spinel precipitates in the metal matrix could introduce significant compressive stresses to squeeze Ni from IOZ to the surface, forming a metallic Ni layer (Fig. S1). It can be demonstrated by comparing the total area of the dislocated Ni with that of internal oxides in Fig. S1. The volume of total Ni (Ni + Ni from NiO) is close to the volume increase because of (Cr, Fe)$_3O_4$ formation. Therefore, the volume expansion due to internal oxide formation coproduced a compressive stress which was the driving force for this Ni transfer. Once the metallic Ni was directly exposed to the high-temperature steam, it would start to be oxidized into NiO on the outer surface, due to the relatively high oxygen partial pressure in the high-temperature steam. Although the oxygen partial pressure in the high-temperature steam environment was high enough to oxidize the metallic Ni directly exposed to it into NiO, the oxygen partial pressure deeper inside the metal matrix should be lower than that at the interface of metal/steam. This explains why Ni inside the metal matrix was not internally oxidized.

The formation of a metallic Ni layer on the original specimen surface was also reported by Xie et al. [56, 101] in the study of the oxidation of Ni-Cr binary alloy in high-temperature wet CO_2. However, the metallic Ni was not observed on the original surface of Fe-17Cr-9Ni steel after exposure to high-temperature steam, although Ni-enrichment was observed in the metal phase of the IOZ [70]. The absence of metallic Ni on the original surface of Fe-17Cr-9Ni steel might be due to its much lower Ni content than that of Fe-21Cr-32Ni steel (9% vs. 32%wt.). The relatively low Ni content of Fe-17Cr-

9Ni steel led to an accumulation of nickel in the metal phase surrounding the internal oxide precipitates, rather than the formation of a nickel layer on the original specimen surface [70]. Although no metallic Ni was expelled to the original surface during the internal oxidation of Fe-17Cr-9Ni steel, the outward diffusion of Fe occurred simultaneously with the internal oxidation, resulting in the formation of an Fe-rich outer oxide layer [70]. However, an outer Fe oxide layer was not observed on Fe-21Cr-32Ni steel after the early-stage oxidation (Fig. S1). This might be because the metallic Ni layer inhibited the outward diffusion of Fe. The slow conversion of Ni to NiO maintained this protection at least for 48h, avoiding Fe-rich oxide formation. It is generally recognised that water vapour is the key factor to lead to the slow kinetics of Ni to NiO in low pO_2 gas atmospheres [56, 101-103].

With the increase of the oxidation time, the volume fraction of the $(Cr, Fe)_3O_4$ spinel is supposed to increase and more metallic Ni would be dislocated to the specimen surface and converted to NiO. Meanwhile the volume fraction of the metal phase in the IOZ decreased and further Ni supply to the specimen surface slowed down.

4.3 *The effect nano-pores on mass transport in the IOZ*

As revealed in Fig. 5, many nanopores with a volume fraction ranging from 5% to 38% were observed in Layer-3 of Fe-21Cr-32Ni steel after 1500h reaction. Similar nano-pores were also observed in Fe-17Cr-9Ni steel (Fig. 13). However, no such nanopores formed when only Ni and NiO on the surface after a short reaction time (Fig. S1). Clearly the volume expansion because of internal oxide formation squeezed Ni out of IOZ but still kept the IOZ dense. Increasing reaction time to 1500h, a thick Fe-rich oxide forms on the top of NiO layer which could be the main reason for void formation due to the fast outward migration of Fe ions through the oxide scale leading to significant vacancy condensation and void formation.

The existence of pores with a micron or submicron scale in the inner oxide layer had been widely reported in ferritic-martensitic steels after exposure to high-temperature steam [15-17, 44, 70, 71], while the nano-sized pores were rarely reported, due to the limited characterization resolution. The formation of the nanopores in Fe-Cr-Ni alloys was supposed to be due to the water dissociation-induced protons promoting the formation, migration, and clustering of both cation and anion vacancies in the oxides [70, 86]. The theory suggested in [70, 86] may also be utilized to explain the development of nanopores in the inner oxide layer of Fe-21Cr-32Ni steel.

The size of the nanopores in the inner oxide layer of Fe-21Cr-32Ni steel ranged from 10 to 50 nm. The volume fraction of the nanopores in the inner oxide layer decreased from the original specimen surface to the oxidation front. This is supposed to be due to a shorter oxidation period in the deeper portion than that in the shallower region. The longer oxidation time in the shallow portion of the inner oxide layer could enable the formation, migration, and clustering of more vacancies.

The high density of nanopores could work as fast-diffusion channels once they were interconnected. Water vapour can present as gas species within these voids to provide the necessary gaseous mass transport, facilitating inward oxygen diffusion [104-107]. This may explain why Ni in Layer-3 was mainly oxidized to form $(Fe, Cr, Ni)_3O_4$ (Figs. 5 and 6). It further demonstrates that the protectiveness of Layer-3 was poor, allowing significant amount of oxygen to go through and increasing oxygen chemical potential in this layer. It is worth noting that not all Ni in Layer-3 was oxidized, and metallic Ni networks was also observed in this layer, implying the variation of oxygen potential in the layer (Figs. 6).

Since Layer-4 was underneath Layer-3, it is reasonable to assume that the oxygen partial pressure in this layer was lower than in Layer-3. This hypothesis is supported by the observation that the oxides in this layer were $(Cr, Fe)_3O_4$ (Figs. 6 and 7), suggesting that the oxygen partial pressure in this layer was not high enough to oxidize Ni. Compared with the metallic Ni networks in Layer-3, the metallic Ni in Layer-4 mainly existed as isolated precipitates (Figs. 6 and 7). The content of metallic Ni in Layer-4 was lower than that in Layer-3 (qualitatively). This might be due to the Ni in this layer was expelled to the outside by the growth of $(Cr, Fe)_3O_4$ while the chromia layer prevent the supplementary of Ni from the underneath region. Although nanopores were also observed in Layer-4, the volume fraction is much lower than that in Layer-3. It was difficult for the low-density nano-cavities in Layer-4 to be interconnected and working as fast-diffusion channels for the gaseous mass. It might be another reason why pO_2 in Layer-4 was lower than that in Layer-3.

In the study of the oxidation of F-M steels in high-temperature steam, it was generally reported that the inner oxide layer (the oxide under the original specimen surface) was mainly composed of nano-sized equiaxed grains [2, 22, 44, 71]. During the oxidation process, the grain boundaries of these nano-sized grains were thought to act as fast-diffusion circuits. However, the nano-sized grains were not observed in the inner oxide layer (Layer-3 and Layer-4) of Fe-21Cr-32Ni steel, and the oxides in Layer-3 and Layer-4 belonged to a same grain (Fig. 11). This grain appeared to have the same crystallographic orientation as the underneath unoxidized matrix grain (Fig. 11). This phenomenon was also observed in Fe-17Cr-9Ni steel, and it was explained to be due to the internal oxides (spinel) retaining the crystallographic orientation of the metal matrix [70]. This may also be the case for Fe-21Cr-32Ni steel. The absence of the grain boundaries of the nano-sized grains in the inner oxide layer (Layer-3 and Layer-4) of Fe-21Cr-32Ni and Fe-17Cr-9Ni steels may suggest that its inner oxide layer might be more protective than that of the F-M steels, regardless of the Cr content and nanopores.

4.4 The effect of Ni networks on elemental diffusion in the IOZ

It is well-known that the elemental diffusion through the lattice of spinel is very slow if the spinel is defect free. Hence, the grain boundaries of the spinel usually work as fast-diffusion channels. The results in the present work show the existence of Ni networks in the inner oxide layer of Fe-21Cr-32Ni and Fe-17Cr-9Ni steels. Similar Ni networks were also observed in surface oxide scales by Zeng et al. [108] in the study of several Fe-Cr-Ni alloys after exposure to a mixed gas of H_2+CO_2+CO+H_2O at 593°C. These authors found that the Ni networks could work as fast-diffusion channels for carbon to transport through the oxide scales, resulting in a fast metal-dusting corrosion. Due to the relatively low pO_2 in the inner oxide layer, Cr and Fe were preferentially oxidized while Ni was expelled to the surrounding region, resulting in the formation of Ni networks similar to that in [108]. Compared with the accelerated carbon in the Ni networks in [108], the inward diffusion of oxygen may also be accelerated through the Ni networks in comparison with through the spinel lattice, which could also decrease the protectiveness of the oxide scales. In addition, it was reported that the interfaces between the internal oxide and the metal matrix could also work as elemental fast-diffusion channels, which could further decrease the protectiveness of the oxide scales [109, 110].

4.5 The internal to external oxidation transition

In the comparative study of the oxidation of 304 steel (Fe-17Cr-9Ni) and HR3C steel (Fe-25Cr-21Ni) in deaerated supercritical water at 600 °C for 1500 h, the results show that 304 steel consistently sustained internal oxidation while HR3C was externally oxidized with a continuous outer Cr_2O_3 oxide scale [83]. For Fe-21Cr-32Ni steel in this work, no external Cr_2O_3 oxide scale formed on the outer surface. However, there was a thin chromia layer identified at the front of the IOZ (Fig. 11). This

observation indicates that this alloy was experiencing the transition from internal to external oxidation at the reaction front where Wagner's criterion met. According to Wagner's theory [111], the internal oxide precipitates would decrease the inward flux of oxygen. The inward flux of oxygen would be reduced further as the volume fraction of the internal oxide precipitates increased. When the inward flow of oxygen falls below a threshold value below which the inward diffusion of oxygen is slower than the outward diffusion of Cr, an internal to external oxidation transition occurs, leading to the growth of a Cr_2O_3 layer (Layer-5) at the oxidation front. The Cr in the Cr_2O_3 layer mainly came from the underneath metal matrix since significant Cr-depletion was observed in these regions (Figs. 1c and 7c). This Cr_2O_3 layer could then work as a diffusion barrier and protect the underneath metal matrix from further oxidation [5, 83]. This internal to external oxidation transition is believed to contribute to the superior corrosion resistance of Fe-21Cr-32Ni steel in high-temperature steam, but it does not happen instantly, requiring more than 48h.

The thicknesses of the oxide scales (excluding the outer oxide layer) grown on Fe-21Cr-32Ni steel, Fe-17Cr-9Ni steel [70], and HR3C steel [83] in 600 °C high-temperature steam for 1500 h were ~7, ~60, and ~0.5 μm, respectively. Because of the low content of Cr in Fe-17Cr-9Ni steel, the transition from internal to external oxidation did not occur during the oxidation period, leading to the growth of a much thicker oxide scale, compared with Fe-21Cr-32Ni steel. The observed internal to external oxidation transition in Fe-21Cr-32Ni steel suggests that the Cr content in this alloy has reached the marginal value for chromia layer formation. Compared with Fe-21Cr-32Ni steel, the oxide scale formed on HR3C was much thinner. These results suggest that the critical chromium concentration for an exclusive chromia formation should be in between the Cr contents of Fe-21Cr-32Ni steel and that of HR3C steel. If the content of Cr is as high as that in HR3C, the outward diffusion rate of Cr could be greater than the inward diffusion rate of oxygen at the beginning, which could completely prevent internal oxidation by forming a continuous outer surface Cr_2O_3 layer [83]. It is worth noting that the average grain size and the minor elements of the three alloys were different, which could also affect the high-temperature oxidation. Hence, the comparison between them can only be treated as qualitative.

Although the Cr_2O_3 layer formed at the oxidation front has been widely reported by many researchers [5, 44, 56, 92, 101], the detailed microstructure of this diffusion barrier layer remains elusive due to the difficulties in obtaining a micro-to-nano scale of observation. The TKD analysis conducted in this study has clearly shown that the Cr_2O_3 layer was mainly composed of nano-grains that were neither equiaxed nor columnar, with some grains elongated along some specific orientations (Fig. 11e). Although there were also nano-sized grains of the Cr_2O_3 oxide formed at the outer surface of HR3C, they had columnar structure, preferentially oriented towards the outer surface [83]. This special orientation of the columnar grains might be because the side growth of the oxide grains is constrained by the surrounding oxide grains, while these constraints were much smaller in the direction towards the outside of the material. Since the Cr_2O_3 band in this study was formed inside the material, the constraints existed in all directions. Hence, if the constraint is the only factor affecting the morphology of the oxide grains, they should have an equiaxed shape. The morphology of the oxide grains observed in this study suggests that the morphology of the oxide grains of Cr_2O_3 band at the oxidation front may also be affected by some other factors, such as the crystallographic orientation of the parental matrix grains.

The results in literature [28, 112, 113] show that the oxide grain boundaries could work as fast-diffusion channels. The preferentially oriented Cr_2O_3 grains on the outer surface in [83] would lead to the formation of grain boundaries that were nearly perpendicular to the specimen surface, resulting in a shortest diffusion path. Compared with the outer Cr_2O_3 oxide scale in [83], the special Cr_2O_3 oxide

grains observed in the present study would increase the total length of the diffusion path, which increased the total time required for the diffusion species to go through the Cr_2O_3 layer. Hence, it is supposed that the Cr_2O_3 layer formed inside the material may have better protectiveness than that formed on the outer specimen surface.

Apart from the Cr_2O_3 layer (Layer-5), there was a semi-continuous layer of SiO_2 (Layer-6) at the metal matrix-Layer-5 interface. A similar SiO_2 layer was also observed in Fe-20Cr and Fe-20Ni-20Cr containing Si in CO_2-rich gas at 650 °C [110], and Ni-20Cr-1Si after exposure to wet [114] and dry CO_2 [115] at 700 °C. It was reported that the SiO_2 layer could significantly reduce the thickness of the internal oxide layer after 500 h of oxidation: ~14 μm in Ni-20Cr, but only ~4 μm in Ni-20Cr-1Si [116]. The formation of the SiO_2 layer underneath the Cr_2O_3 band was because SiO_2 was thermodynamically more stable at the low oxygen activity set by the Cr_2O_3-metal matrix interfacial equilibrium [116]. Given the similarities in the SiO_2 layer identified in this study and in [113-116], it is reasonable to believe that the SiO_2 layer in this study could also act as a diffusion barrier and decrease the oxidation rate of Fe-21Cr-32Ni steel. It is worth noting that the SiO_2 layers in [113-116] were all reported to be amorphous, which may explain why the SiO_2 layer in this study cannot be indexed by the TKD (Fig. 11).

4.6 The formation of a duplex outer oxide layer

The morphology and chemical composition of the surface oxide scale grown on Fe-21Cr-32Ni steel after 1500 h were very different from that oxidized for 48 h. The metallic Ni layer formed after 48 h of exposure completely disappeared after 1500 h of exposure and was replaced by a duplex outer oxide layer: a NiO layer (Layer-2) and a $NiFe_2O_4$ layer (Layer-1). The formation of the NiO layer could be due to the longer time exposure, resulting in full oxidation of the initially formed metallic Ni layer. This hypothesis is supported by the observation that the metallic Ni layer had started to be oxidized after the early-stage oxidation (Fig. S1). Apart from the NiO layer, there was an outermost $NiFe_2O_4$ layer (Layer-1) just above the NiO layer (Layer-2). This oxide layer was not observed at the early-stage oxidation. It is supposed in this study that the outward diffusion of Fe would occur after the metallic Ni layer had been converted to NiO. Unlike pure Ni, NiO is a typical p-type metal-deficit semiconductor with high cation vacancies and positive holes which benefit for Fe ion diffusion [103]. Also as revealed in this work (Fig. 10), NiO in Layer 2 is very fine. The grain boundaries of the nano-sized NiO (Fig. 10) could act as fast-diffusion channels [28, 117] and then facilitate the outward Fe ions diffusion through the NiO layer, resulting in the formation of the $NiFe_2O_4$ layer according to Equation (1) [50]:

$$NiO + 2Fe + (3/2)O_2 = NiFe_2O_4 \quad (1)$$

In the study of the oxidation of Ni-20Cr-5Fe steel in wet CO_2 at 700 °C for 500h, a triplex outer oxide layer was observed on the original specimen surface, including an innermost metallic Ni layer, a medium NiO layer, and an outermost $NiFe_2O_4$ layer [92]. The formation of the NiO layer was also believed to be due to the oxidation of the innermost metallic Ni layer [92], and the outermost $NiFe_2O_4$ layer formed according to Equation (1).

The observation of the co-existence of NiO and $NiFe_2O_4$ in the same grains and the irregular interfaces between the two oxides in the present study (Fig. 10) further proves that the formation of the $NiFe_2O_4$ layer was due to the consumption of the NiO layer. It is worth noting that the two oxides have a Face Centred Cubic (FCC) structure. Although their lattice parameters are different: 0.4195 nm in NiO [118] and 0.8359 nm in $NiFe_2O_4$ [119], they have similar atomic arrangements. The results in this study

show that it is possible for the two oxides to co-exist in the same oxide grains, due to their similar crystallographic structure and correlated lattice size. Although the atomic structure of the NiO-$NiFe_2O_4$ interface is not examined in this study, a certain amount of stress at the interface can be expected, considering the lattice mismatches between the two phases, which might contribute to the oxide scale exfoliation after a longer time oxidation.

5. Conclusions

1. A 5-layered surface oxide scale was observed on Fe-21Cr-32Ni steel after exposure to steam at 600 ℃ for 1500 h. By comparing with the oxide scale formed after 48 h of exposure, it is shown that this steel was oxidized under the internal oxidation mechanism at the early stage of exposure. After a longer time of exposure, the oxidation mechanism transferred from internal oxidation to external oxidation. In comparison, the lower Cr content in Fe-17Cr-9Ni steel is not enough to support the formation of a continuous chromia layer at the oxidation front. Hence, the internal oxidation mechanism sustained during the whole period of exposure.

2. Compared with Fe-17Cr-9Ni steel, the superior corrosion-resistance of Fe-21Cr-32Ni steel has been demonstrated to be mainly due to the formation of a continuous chromia layer, which could effectively block the inward diffusion of oxygen and the outward diffusion of metallic ions. The chromia layer was composed of nano-sized grains that were neither equiaxed nor columnar, with some grains elongated along some specific orientations. The special morphologies of the nano-sized grains could increase the total length of the diffusion paths and decrease the oxidation rate. The formation of a semi-continuous silica layer at the oxidation front and the expulsion of metallic Ni onto the specimen surface, forming a continuous metallic Ni layer, are also believed to contribute to the superior corrosion-resistance of this steel.

3. The inner oxide layer of Fe-21Cr-32Ni and Fe-17Cr-9Ni steels were all nano-porous, which was supposed to be due to the outward Fe ions diffusion and water dissociation-induced protons promoting the formation, migration, and clustering of both cation and anion vacancies in the oxides. The volume fraction of the nanopores decreased in the direction towards the inside of the material. The high-volume fraction of nano-pores was believed to be able to act as fast-diffusion channels for gaseous mass transport in the IOZ. This is because Ni was always observed to be oxidized in the region where nanopores were enriched.

4. Ni networks are observed in the IOZ of Fe-17Cr-9Ni and Fe-21Cr-32Ni steels. The formation of the Ni networks in the IOZ is believed to be due to the preferential oxidation of Cr and Fe resulting in the Ni expulsion. These Ni networks and the metallic Ni-oxide interfaces could work as fast-diffusion channels to accelerate cation diffusion.

Acknowledgements

This work was supported by the National Key Research and Development Program of China (YS2018YFE010246). EPSRC (EP/K040375/1, EP/N010868/1, and EP/R009392/1) and National Nature Science Foundation of China (U2032121) grants are also acknowledged for funding this research. Prof. Lefu Zhang is acknowledged for providing the samples used in this study. Microstructural Characterization of Instrumental Analysis Center of SJTU is also gratefully acknowledged. The atom probe facilities at the University of Oxford are funded by the EPSRC (EP/M022803/1). BMJ would like to acknowledge funding from EPSRC program grant MIDAS (EP/S01702X/1).

References

[1] C. Cabet, F. Dalle, E. Gaganidze, J. Henry, H. Tanigawa, Ferritic-martensitic steels for fission and fusion applications. J. Nucl. Mater., 523(2019) 510-537.

[2] I.G. Wright, R.B. Dooley, A review of the oxidation behaviour of structural alloys in steam. Int. Mater. Rev., 55(2010) 129-167.

[3] S.R.J. Saunders, M. Monteiro, F. Rizzo, The oxidation behaviour of metals and alloys at high temperatures in atmospheres containing water vapour: A review. Prog. Mater. Sci., 53(2008) 775-837.

[4] N. Birks, G.H. Meier, F.S. Pettit, Introduction to the high temperature oxidation of metals. Cambridge University Press, 2006.

[5] D.J. Young, High temperature oxidation and corrosion of metals. Vol. 1., Elsevier, 2008.

[6] T. Yang, X. Liu, X. Cheng. Optimization of multilayer fuel assemblies for supercritical water-cooled reactors with mixed neutron spectrum. Nuclear engineering and design, 249(2012) 159-165.

[7] J. Hofmeister, C. Waata, J. Starflinger, T. Schulenberg, E. Laurien. Fuel assembly design study for a reactor with supercritical water. Nuclear Engineering and Design, 237(2007) 1513-1521.

[8] R. Viswanathan, J. F. Henry, J. Tanzosh, G. Stanko, J. Shingledecker, B. Vitalis, R. Purgert. US program on materials technology for ultra-supercritical coal power plants. Journal of materials engineering and performance 14 (2005) 281-292.

[9] Chunwen Sun, Rob Hui, Wei Qu, Sing Yick. Progress in corrosion resistant materials for supercritical water reactors. Corrosion Science, 51(2009): 2508-2523.

[10] R. Viswanathan, J. Sarver, J.M. Tanzosh, Boiler materials for ultra-supercritical coal power plants—steam side oxidation. J. Mater. Eng. Perform., 15(2006) 255-274.

[11] F. Abe, Precipitate design for creep strengthening of 9% Cr tempered martensitic steel for ultra-supercritical power plants. Sci. Technol. Adv. Mater., 9(2008) 013002.

[12] S.J. Zinkle, G.S. Was, Materials challenges in nuclear energy. Acta Mater., 61(2013) 735-758.

[13] Y. Li, T. Xu, S. Wang, J. Yang, B. Fekete, J. Yang, A. Wu, J. Qiu, Y. Xu, D.D. Macdonald, Predictions and Analyses on the Growth Behavior of Oxide Scales Formed on Ferritic–Martensitic in Supercritical Water. Oxid. Met., 92(2019) 27-48.

[14] L. Zhang, Y. Bao, R. Tang, Selection and corrosion evaluation tests of candidate SCWR fuel cladding materials. Nucl. Eng. Des., 249(2012) 180-187.

[15] L. Tan, X. Ren, T.R. Allen, Corrosion behavior of 9–12% Cr ferritic–martensitic steels in supercritical water. Corros. Sci., 52(2010) 1520-1528.

[16] Y. Chen, K. Sridharan, T. Allen, Corrosion behavior of ferritic–martensitic steel T91 in supercritical water. Corros. Sci., 48(2006) 2843-2854.

[17] J. Ehlers, D.J. Young, E.J. Smaardijk, A.K. Tyagi, H.J. Penkalla, L. Singheiser, W.J. Quadakkers. Enhanced oxidation of the 9% Cr steel P91 in water vapour containing environments. Corros. Sci., 48(2006) 3428-3454.

[18] J. Bischoff, A.T. Motta, EFTEM and EELS analysis of the oxide layer formed on HCM12A exposed to SCW. J. Nucl. Mater., 430(2012) 171-180.

[19] I. Betova, M. Bojinov, P. Kinnunen, V. Lehtovuori, S. Peltonen, S. Penttilä, T. Saario, Composition, structure, and properties of corrosion layers on ferritic and austenitic steels in ultrasupercritical water. J. Electrochem. Soc., 153(2006) B464-B473.

[20] W.H. Yeo, A.T. Fry, J. Purbolaksono, S. Ramesh, J.I. Inayat-Hussain, H.L. Liew, M. Hamdi, Oxide scale growth and presumed exfoliation in a 700 C or higher steam condition: A simulation study for future operations of ultra-supercritical power plants. J. Supercrit. Fluids, 92(2014) 215-222.

[21] M.F. Montemor, M.G.S. Ferreira, N.E. Hakiki, M.D.C. Belo, Chemical composition and electronic structure of the oxide films formed on 316L stainless steel and nickel based alloys in high temperature aqueous environments. Corros. Sci., 42(2000) 1635-1650.

[22] G.S. Was, P. Ampornrat, G. Gupta, S. Teysseyre, E.A. West, T.R. Allen, K. Sridharan, L. Tan, Y. Chen, X. Ren, C. Pister, Corrosion and stress corrosion cracking in supercritical water. J. Nucl. Mater., 371(2007) 176-201.

[23] Y. Behnamian, A. Mostafaei, A. Kohandehghan, B.S. Amirkhiz, J. Li, W. Zheng, D. Guzonas, M. Chmielus, W. Chen, J.L. Luo, Characterization of oxide layer and micro-crack initiation in alloy 316L stainless steel after 20,000 h exposure to supercritical water at 500° C. Mater. Charact., 131(2017), 532-543.

[24] X. Guo, K. Chen, W. Gao, Z. Shen, P. Lai, L. Zhang. A research on the corrosion and stress corrosion cracking susceptibility of 316L stainless steel exposed to supercritical water. Corros. Sci., 127(2017) 157-167.

[25] G.S. Was, S. Teysseyre, Z. Jiao. Corrosion of austenitic alloys in supercritical water. Corrosion, 62(2006) 989-1005.

[26] M. Nezakat, H. Akhiani, S. Penttilä, S.M. Sabet, J. Szpunar. Effect of thermo-mechanical processing on oxidation of austenitic stainless steel 316L in supercritical water. Corros. Sci., 94(2015), 197-206.

[27] S. Cissé, L. Laffont, B. Tanguy, M.C. Lafont, E. Andrieu, Effect of surface preparation on the corrosion of austenitic stainless steel 304L in high temperature steam and simulated PWR primary water. Corros. Sci., 56(2012) 209-216.

[28] J. Yuan, X. Wu, W. Wang, S. Zhu, F. Wang, The effect of surface finish on the scaling behavior of stainless steel in steam and supercritical water. Oxid. Met., 79(2013) 541-551.

[29] Z. Shen, M. Meisnar, K. Arioka, S. Lozano-Perez, Mechanistic understanding of the temperature dependence of crack growth rate in alloy 600 and 316 stainless steel through high-resolution characterization. Acta Mater., 165(2019) 73-86.

[30] X. Zhong, E.H. Han, X. Wu, Corrosion behavior of Alloy 690 in aerated supercritical water. Corros. Sci., 66(2013) 369-379.

[31] Y. Behnamian, A. Mostafaei, A. Kohandehghan, B.S. Amirkhiz, D. Serate, Y. Sun, S. Liu, E. Aghaie, Y. Zeng, M. Chmielus, W. Zheng, A comparative study of oxide scales grown on stainless steel and nickel-based superalloys in ultra-high temperature supercritical water at 800 C. Corros. Sci., 106(2016) 188-207.

[32] X. Guo, Y. Fan, W. Gao, R. Tang, K. Chen, Z. Shen, L. Zhang. Corrosion resistance of candidate cladding materials for supercritical water reactor. Annals of Nuclear Energy, 127(2019) 351-363.

[33] X. Luo, R. Tang, C. Long, Z. Miao, Q. Peng, C. Li. Corrosion behavior of austenitic and ferritic steels in supercritical water. Nuclear Engineering and Technology, 40(2008) 147-154.

[34] X. Guo, K. Chen, W. Gao, Z. Shen, L. Zhang. Corrosion behavior of alumina-forming and oxide dispersion strengthened austenitic 316 stainless steel in supercritical water. Corrosion Science, 138(2018) 297-306.

[35] Z. Shen, L. Zhang, R. Tang, Q. Zhang. The effect of temperature on the SSRT behavior of austenitic stainless steels in SCW. Journal of Nuclear Materials, 454(2014) 274-282.

[36] Z. Shen, L. Zhang, R. Tang, Q. Zhang. SCC susceptibility of type 316Ti stainless steel in supercritical water. Journal of Nuclear Materials, 458(2015) 206-215.

[37] D. G˘mez-Brice, F. Blßzquez, A. Sßez-Maderuelo. Oxidation of austenitic and ferritic/martensitic alloys in supercritical water. The Journal of Supercritical Fluids, 78(2013) 103-113.

[38] Y. Behnamian, A. Mostafaei, A. Kohandehghan, B. Zahiri, W. Zheng, D. Guzonas, M. Chmielus, W. Chen, J.L. Luo. Corrosion behavior of alloy 316L stainless steel after exposure to supercritical water at 500° C for 20,000 h. The Journal of Supercritical Fluids, 127(2017) 191-199.

[39] Y. Li, S. Wang, P. Sun, D. Xu, M. Ren, Y. Guo, G. Lin. Early oxidation mechanism of austenitic stainless steel TP347H in supercritical water. Corrosion Science, 128(2017) 241-252.

[40] S. Penttilä, A. Toivonen, J. Li, W. Zheng, R. Novotny. Effect of surface modification on the corrosion resistance of austenitic stainless steel 316L in supercritical water conditions. The Journal of Supercritical Fluids, 81(2013) 157-163.

[41] R. Novotny, P. Hähner, J. Siegl, P. Haušild, S. Ripplinger, S. Penttilä, A. Toivonen. Stress corrosion cracking susceptibility of austenitic stainless steels in supercritical water conditions. Journal of Nuclear Materials, 409(2011) 117-123.

[42] X. Gao, X. Wu, Z. Zhang, H. Guan, E.H. Han. Characterization of oxide films grown on 316L stainless steel exposed to H2O2-containing supercritical water. The Journal of supercritical fluids, 42(2007) 157-163.

[43] H. Chen, R. Tang, C. Long, G. Le. Effect of exposure temperature on the corrosion behaviors of TP347H austenitic stainless steel in supercritical water. Corrosion Science, 161(2019) 108188.

[44] K. Chen, L. Zhang, Z. Shen. Understanding the surface oxide evolution of T91 ferritic-martensitic steel in supercritical water through advanced characterization. Acta Materialia, 194(2020) 156-167.

[45] L. Tan, X. Ren, T.R. Allen. Corrosion behavior of 9–12% Cr ferritic–martensitic steels in supercritical water. Corrosion science, 52(2010) 1520-1528.

[46] L. Tan, M.T. Machut, K. Sridharan, T.R. Allen. Corrosion behavior of a ferritic/martensitic steel HCM12A exposed to harsh environments. Journal of Nuclear Materials, 371(2007) 161-170.

[47] L. Sun, W.P. Yan. Estimation of oxidation kinetics and oxide scale void position of ferritic-martensitic steels in supercritical water. Adv. Mater. Sci. Eng. (2017) 1-12.

[48] N.Q. Zhang, H. Xu, B.R. Li, Y. Bai, D.Y. Liu. Influence of the dissolved oxygen content on corrosion of the ferritic–martensitic steel P92 in supercritical water. Corrosion science, 56(2012) 123-128.

[49] J. Bischoff, A.T. Motta, C. Eichfeld, R.J. Comstock, G. Cao, T.R. Allen. Corrosion of ferritic–martensitic steels in steam and supercritical water. Journal of Nuclear Materials, 441(2013) 604-611.

[50] X. Zhong, X. Wu, E.H. Han. Effects of exposure temperature and time on corrosion behavior of a ferritic–martensitic steel P92 in aerated supercritical water. Corrosion Science, 90(2015) 511-521.

[51] Z. Zhu, H. Xu, D. Jiang, X. Mao, N. Zhang. Influence of temperature on the oxidation behaviour of a ferritic-martensitic steel in supercritical water. Corrosion Science, 113(2016) 172-179.

[52] X. Zhong, X. Wu, E.H. Han. The characteristic of oxide scales on T91 tube after long-term service in an ultra-supercritical coal power plant. The Journal of Supercritical Fluids, 72(2012) 68-77.

[53] X. Ren, K. Sridharan, T.R. Allen. Corrosion of ferritic–martensitic steel HT9 in supercritical water. Journal of Nuclear Materials, 358(2006) 227-234.

[54] H. Hu, Z. Zhou, M. Li, L. Zhang, M. Wang, S. Li, C. Ge. Study of the corrosion behavior of a 18Cr-oxide dispersion strengthened steel in supercritical water. Corrosion science, 65(2012) 209-213.

[55] G.B. Gibbs, A model for mild steel oxidation in CO_2. Oxid. Met., 7(1973) 173-184.

[56] Y. Xie, J. Zhang, D.J. Young, Water vapour effects on corrosion of Ni-Cr alloys in CO_2 gas at 650° C. Corros. Sci., 136(2018) 311-325.

[57] L.F. He, P. Roman, B. Leng, K. Sridharan, M. Anderson, T.R. Allen, Corrosion behavior of an alumina forming austenitic steel exposed to supercritical carbon dioxide. Corros. Sci., 82(2014) 67-76.

[58] G. Cao, V. Firouzdor, K. Sridharan, M. Anderson, T. R. Allen. Corrosion of austenitic alloys in high temperature supercritical carbon dioxide. Corrosion Science, 60(2012) 246-255.

[59] V. Firouzdor, K. Sridharan, G. Cao, M. Anderson, T. R. Allen. Corrosion of a stainless steel and nickel-based alloys in high temperature supercritical carbon dioxide environment. Corrosion Science, 69(2013) 281-291.

[60] A. Alemberti, V. Smirnov, C. F. Smith, M. Takahashi. Overview of lead-cooled fast reactor activities. Progress in Nuclear Energy, 77(2014) 300-307.

[61] P. Hosemann, R. Dickerson, P. Dickerson, N. Li, S.A. Maloy, Transmission electron microscopy (TEM) on oxide layers formed on D9 stainless steel in lead bismuth eutectic (LBE). Corros. Sci., 66(2013) 196-202.

[62] L. Martinelli, F. Balbaud-Célérier, A. Terlain, S. Delpech, G. Santarini, J. Favergeon, G. Moulin, M. Tabarant, G. Picard, Oxidation mechanism of a Fe–9Cr–1Mo steel by liquid Pb–Bi eutectic alloy (Part I). Corros. Sci., 50(2008) 2523-2536.

[63] L. Martinelli, F. Balbaud-Célérier, A. Terlain, S. Bosonnet, G. Picard, G. Santarini, Oxidation mechanism of an Fe–9Cr–1Mo steel by liquid Pb–Bi eutectic alloy at 470 C (Part II). Corros. Sci., 50(2008) 2537-2548.

[64] C. Wagner. The distribution of cations in metal oxide and metal sulphide solid solutions formed during the oxidation of alloys. Corrosion Science, 9(1969) 91-109.

[65] R. Dieckmann. Defects and cation diffusion in magnetite (IV): Nonstoichiometry and point defect structure of magnetite (Fe3-δO4). Berichte der Bunsengesellschaft für physikalische Chemie, 86(1982) 112-118.

[66] J. Töpfer, S. Aggarwal, R. Dieckmann. Point defects and cation tracer diffusion in (CrxFe1− x) 3− δO4 spinels. Solid State Ionics, 81(1995) 251-266.

[67] J. Bischoff, A.T. Motta, Oxidation behavior of ferritic–martensitic and ODS steels in supercritical water. J. Nucl. Mater., 424(2012) 261-276.

[68] A. Atkinson, Surface and interface mass transport in ionic materials. Solid State Ionics, 28–30 (1988) 1377-1387.

[69] J. Robertson, The mechanism of high temperature aqueous corrosion of stainless steels. Corros. Sci., 32 (1991) 443-465.

[70] Z. Shen, D. Tweddle, H. Yu, G. He, A. Varambhia, P. Karamched, F. Hofmann, A.J. Wilkinson, M.P. Moody, L. Zhang, S. Lozano-Perez. Microstructural understanding of the oxidation of an austenitic stainless steel in high-temperature steam through advanced characterization. Acta Materialia, 194(2020) 321-336.

[71] Z. Shen, K. Chen, H. Yu, B. Jenkins, Y. Ren, N. Saravanan, G. He, X. Luo, P.A. Bagot, M.P. Moody, L. Zhang. New insights into the oxidation mechanisms of a Ferritic-Martensitic steel in high-temperature steam. Acta Materialia, 194(2020) 522-539.

[72] D. Du, K. Chen, L. Zhang, Z. Shen. Microstructural investigation of the nodular corrosion of 304NG stainless steel in supercritical water. Corrosion Science, 170(2020) 108652.

[73] L. Tan, K. Sridharan, T.R. Allen. The effect of grain boundary engineering on the oxidation behavior of INCOLOY alloy 800H in supercritical water. Journal of nuclear materials, 348(2006) 263-271.

[74] L. Tan, X. Ren, K. Sridharan, T.R. Allen. Effect of shot-peening on the oxidation of alloy 800H exposed to supercritical water and cyclic oxidation. Corrosion Science, 50(2008) 2040-2046.

[75] L. Tan, T.R. Allen, Y. Yang. Corrosion behavior of alloy 800H (Fe–21Cr–32Ni) in supercritical water. Corrosion Science, 53(2011) 703-711.

[76] K.I. Choudhry, S. Mahboubi, G.A. Botton, J.R. Kish, I.M. Svishchev. Corrosion of engineering materials in a supercritical water cooled reactor: Characterization of oxide scales on Alloy 800H and stainless steel 316. Corrosion Science, 100(2015) 222-230.

[77] S. Bsat, B. Xiao, X. Huang, S. Penttilä. Oxidation behaviour of alloys 800H, 3033 and 304 in high-temperature supercritical water. Oxidation of Metals, 89(2018) 151-163.

[78] H. Akhiani, M. Nezakat, S. Penttilä, J. Szpunar. The oxidation resistance of thermo-mechanically processed Incoloy 800HT in supercritical water. The Journal of Supercritical Fluids, 101(2015) 150-160.

[79] K.I. Choudhry, D.A. Guzonas, D.T. Kallikragas, I.M. Svishchev. On-line monitoring of oxide formation and dissolution on alloy 800H in supercritical water. Corrosion Science, 111(2016) 574-582.

[80] Z. Shen, K. Chen, X. Guo, L. Zhang. A study on the corrosion and stress corrosion cracking susceptibility of 310-ODS steel in supercritical water. Journal of Nuclear Materials, 514(2019) 56-65.

[81] F. Liu, J. E. Tang, H. Asteman, J. E. Svensson, L. G. Johansson, M. Halvarsson. Investigation of the evolution of the oxide scale formed on 310 stainless steel oxidized at 600° C in oxygen with 40% water vapour using FIB and TEM. Oxidation of metals, 71(2009) 77-105.

[82] H. Asteman, J. E. Svensson, L. G. Johansson. Oxidation of 310 steel in H2O/O2 mixtures at 600 C: the effect of water-vapour-enhanced chromium evaporation. Corrosion Science, 44(2002) 2635-2649.

[83] K. Chen, L. Zhang, S. Wu, Z. Shen. High-resolution characterization of the internal and external oxidation of austenitic alloys in supercritical water. Scripta Materialia, 197(2021) 113814.

[84] J. Yuan, W. Wang, H. Zhang, L. Zhu, S. Zhu, F. Wang. Investigation into the failure mechanism of chromia scale thermally grown on an austenitic stainless steel in pure steam. Corrosion Science, 109(2016) 36-42.

[85] Z. Zhu, H. Xu, H. I. Khan, D. Jiang, N. Zhang. Effect of exposure temperature on oxidation of austenitic steel HR3C in supercritical water. Oxidation of Metals, 91(2019) 77-93.

[86] L. Luo, M. Su, P. Yan, L. Zou, D.K. Schreiber, D.R. Baer, Z. Zhu, G. Zhou, Y. Wang, S.M. Bruemmer, Z. Xu. Atomic origins of water-vapour-promoted alloy oxidation. Nature materials, 17(2018) 514-518.

[87] D.G. Xie, Z.J. Wang, J. Sun, J. Li, E. Ma, Z.W. Shan. In situ study of the initiation of hydrogen bubbles at the aluminium metal/oxide interface. Nature materials, 14(2015)c899-903.

[88] A. King, G. Johnson, D. Engelberg, W. Ludwig, J. Marrow. Observations of intergranular stress corrosion cracking in a grain-mapped polycrystal. Science, 321(2008) 382-385.

[89] T.L. Burnett, P.J. Withers. Completing the picture through correlative characterization. Nature materials, 18(2019) 1041-1049.

[90] Z. Shen, J. Dohr, S. Lozano-Perez. The effects of intergranular carbides on the grain boundary oxidation and cracking in a cold-worked Alloy 600. Corrosion Science, 155(2019) 209-216.

[91] G.S. Was, S. Teysseyre, Z. Jiao, Corrosion of austenitic alloys in supercritical water, Corrosion, 62 (2006) 989-1005.

[92] Y. Xie, J. Zhang, D.J. Young, W. Zheng. Effect of Fe on corrosion of Ni-20Cr and Ni-30Cr alloys in wet CO2 gas at 650 and 700° C. Corrosion Science, 154(2019) 129-143.

[93] B. Langelier, S.Y. Persaud, R.C. Newman, G.A. Botton. An atom probe tomography study of internal oxidation processes in Alloy 600. Acta Materialia, 109(2016) 55-68.

[94] H.C. Yi, S.W. Guan, W.W. Smeltzer, A. Petric. Internal oxidation of Ni-Al and Ni-Al-Si alloys at the dissociation pressure of NiO. Acta Metallurgica et Materialia, 42(1994) 981-990.

[95] G. Bertali, F. Scenini, M.G. Burke. The effect of residual stress on the Preferential Intergranular Oxidation of Alloy 600. Corrosion Science, 111(2016) 494-507.

[96] J. Chen, C. Jang, Q. Xiao, H.B. Lee, C. Kim, S.H. Kim, J.H. Shin, G.O. Subramanian. Effect of surface conditions and alloying elements on the early oxidation behaviour of two austenitic alloys in the pure steam environment. Applied Surface Science, 563(2021) 150314.

[97] C.W. Bale, P. Chartrand, S.A. Degterov, G. Eriksson, K. Hack, R.B. Mahfoud, J. Melançon, A.D. Pelton, S. Petersen. FactSage thermochemical software and databases. Calphad, 26(2002) 189-228.

[98] A. Rahmel, J. Tobolski. Einfluss von wasserdampf und kohlendioxyd auf die oxydation von eisen in sauerstoff bei hohen temperaturen. Corrosion Science, 5(1965) 333-346.

[99] C.T. Fujii, R.A. Meussner. Oxide Structures Produced on Iron - Chromium Alloys by a Dissociative Mechanism. Journal of the Electrochemical Society, 110(1963) 1195-1204.

[100] T. Terachi, Yamada, T., Miyamoto, T., Arioka, K. and Fukuya, K., 2008. Corrosion behavior of stainless steels in simulated PWR primary water—effect of chromium content in alloys and dissolved hydrogen—. Journal of nuclear science and technology, 45(10) 975-984.

[101] Y. Xie, T.D. Nguyen, J. Zhang, D.J. Young, Corrosion behaviour of Ni-Cr alloys in wet CO2 atmosphere at 700 and 800 °C, Corros. Sci., 146 (2019) 28-43.

[102] E. Essuman, G.H. Meier, J. Zurek, M. Hänsel, T. Norby, L. Singheiser, W.J. Quadakkers, Protective and non-protective scale formation of NiCr alloys in water vapour containing high- and low-pO2 gases, Corros. Sci., 50 (2008) 1753-1760.

[103] A. Galerie, Y. Wouters, M. Caillet, The kinetic behaviour of metals in water vapour at high temperatures: can general rules be proposed?, Mater. Sci. Forum., 369-372 (2001) 231-238.

[104] C. T. Fujii, R. A. Meussner. The Mechanism of the High - Temperature Oxidation of Iron - Chromium Alloys in Water Vapor. Journal of the Electrochemical Society, 111(1964) 1215-1221.

[105] A. Rahmel, J. Tobolski. Influence of water vapor and carbon dioxide on the oxidation of iron in oxygen at high temperatures. Corros. Sci., 5(1965) 333-346.

[106] T. Maruyama, N. Fukagai, M. Ueda, K. Kawamura. Chemical potential distribution and void formation in magnetite scale formed in oxidation of iron at 823K. Materials Science Forum, 461(2004) 807-814.

[107] M. Ueda, K. Kawamura, T. Maruyama. Void formation in magnetite scale formed on iron at 823 K-Elucidation by chemical potential distribution. Materials Science Forum, 522(2006) 37-44.

[108] Z. Zeng, K. Natesan, Z. Cai, S. B. Darling. The role of metal nanoparticles and nanonetworks in alloy degradation. Nature Materials, 7(2008) 641-646.

[109] D.P. Whittle, Y. Shida, G.C. Wood, F. H. Stott, B. D. Bastow. Enhanced diffusion of oxygen during internal oxidation of nickel-base alloys. Philosophical Magazine A, 46(1982) 931-949.

[110] A. Martinez-Villafane, F.H. Stott, J.G. Chacon-Nava, G.C. Wood. Enhanced oxygen diffusion along internal oxide–metal matrix interfaces in Ni–Al alloys during internal oxidation. Oxidation of metals, 57(2002) 267-279.

[111] C. Wagner. Reaktionstypen bei der Oxydation von Legierungen, Z. Elektrochem., 63 (1959) 772-782.

[112] N. Mortazavi, C. Geers, M. Esmaily, V. Babic, M. Sattari, K. Lindgren, P. Malmberg, B. Jönsson, M. Halvarsson, J.E. Svensson, I. Panas, Interplay of water and reactive elements in oxidation of alumina-forming alloys, Nat. Mater., 17(2018) 610-617.

[113] T.D. Nguyen, J. Zhang, D.J. Young, Effects of Silicon and Water Vapour on Corrosion of Fe-20Cr and Fe-20Cr-20Ni Alloys in CO2 at 650°C, Oxidation of Metals, 87 (2017) 541-573.

[114] T.D. Nguyen, J. Zhang, D.J. Young. Effects of Si, Al and Ti on corrosion of Ni-20Cr and Ni-30Cr alloys in Ar-20CO2-20H2O gas at 700° C. Corrosion Science, 170(2020) 108702.

[115] T.D. Nguyen, J. Zhang, D.J. Young. Effects of Si, Al and Ti on corrosion of Ni-20Cr and Ni-30Cr alloys in Ar-20CO2 at 700° C. Corrosion Science, 130(2018) 161-176.

[116] T.D. Nguyen, J. Zhang, D.J. Young. Effects of silicon on high temperature corrosion of Fe–Cr and Fe–Cr–Ni alloys in carbon dioxide. Oxidation of metals, 81(2014) 549-574.

[117] N. Mortazavi, C. Geers, M. Esmaily, V. Babic, M. Sattari, K. Lindgren, P. Malmberg, B. Jönsson, M. Halvarsson, J.E. Svensson, I. Panas, Interplay of water and reactive elements in oxidation of alumina-forming alloys, Nat. Mater., 17(2018) 610-617.

[118] I. Hotovy, J. Huran, L. Spiess. Characterization of sputtered NiO films using XRD and AFM. Journal of materials science, 39(2004) 2609-2612.

[119] A. Kremenović, B. Antić, M. Vučinić-Vasić, P. Colomban, Č. Jovalekić, N. Bibić, V. Kahlenberg, M. Leoni. Temperature-induced structure and microstructure evolution of nanostructured Ni0. 9Zn0. 1O. Journal of Applied Crystallography, 43(2010) 699-709.